OEB Univ. Publish. Co.

Transmission Line Matrix: A Tool for Modeling Thermo-Electric properties of Materials and Devices

A. Saidane*, S. Mimouni and R. Houcine

CaSiCCE Laboratory, ENSET-Oran, B.P 1523 M'Naouer-Oran, Algeria
* Email: saidaneaek@yahoo.com

Abstract

Transmission-Line-Matrix (TLM) method, originally developed in 1971 as a numerical technique for modeling electromagnetic wave propagation, has since been established as a powerful technique to study diffusion problems, vibration, heat transfer, electromagnetic compatibility, radar, etc. The TLM method is a time and space discrete method that solves field problems using their circuit equivalent. It assembles a lattice of discrete points in space as one-dimensional lines and defines the transmission matrix between lattice points, so that successive calculations can be performed. The physical variable is modeled as a sequence of voltage pulses travelling through this network of transmission lines. The TLM routine operates on the travelling, scattering, and connecting of these pulses in the network. The transmission lines in the model act as delay lines, with the node impulse population being the discrete solution at each time step.

TLM is a discrete model which can be solved exactly since approximations are only introduced at the discretisation stage. This is to be contrasted with the traditional approach in which an idealized continuous model is first obtained and then this model is solved approximately. It main advantages are that, it is intuitive and can be simply formulated, explicit, unconditionally stable since it is a passive network which is solved exactly, can be used to model arbitrary and complex structures, inhomogeneous media can be modeled very conveniently, and the impulse response and time domain performance of the system can be obtain straightforwardly.

TLM method is used to model self-heating in various two electronic devices and structures: AlGaN/GaN power transistors and insulated gate bipolar transistor (IGBT) modules. Results show that the method is well suited for understanding heat management in microelectronic devices and gives insights for future designs.

Key words *TLM ; Modeling ; Self-heating ; power transistors ; IGBT modules*

1. Introduction

Transmission-Line-Matrix (TLM) method, originally developed in 1971 as a numerical technique for modeling electromagnetic wave propagation [1], has since been established as a powerful technique to study diffusion problems [2-4], vibration [5,6], heat transfer [7,8], electromagnetic compatibility [9], radar [10], etc. It is based on Huygens principle and could be used for modeling any phenomena which obeys this principle. It is a time and space discrete method that solves field problems using their electrical circuit equivalent. It assembles a lattice of discrete points in space connected by transmission lines and defines the transmission matrix between lattice points, so that successive calculations can be performed. Transmission-lines are considered as distributed models of capacitors, inductors and resistors. The user therefore has a good grasp of the properties and behavior of the model, the nature and significance of errors and the manner in which material properties may be introduced. The physical variable is modeled as a sequence of voltage pulses travelling through this network of transmission lines to become incident simultaneously on all parts of all nodes. These incident pulses are scattered instantaneously into reflected pulses which, during the time step **Δ**, travel along link transmission lines to become incident upon neighboring nodes. The TLM routine operates on the travelling, scattering, and connecting of these pulses in the network. The transmission lines in the model act as delay lines, with the node impulse population being the discrete solution at each time step.

TLM is a discrete model which can be solved exactly since approximations are only introduced at the discretisation stage. This is to be contrasted with the traditional approach in which an idealized continuous model is first obtained and then this model is solved approximately. It main advantages are that, it is intuitive and can be simply formulated, explicit, unconditionally stable since it is a passive network which is solved exactly, can be used to model arbitrary and complex structures. Inhomogeneous media can be modeled very conveniently, and the impulse response and time domain performance of the system can be obtain straightforwardly.

In this communication, the TLM method is explained and used to model self-heating in various electronic devices and structures. Results show that the method is well suited for understanding heat management in microelectronic devices and gives insights for future devices designs.

2. TLM model

To obtain rise in temperature of device structure, we solve the heat-flow nonlinear equation:

$$\nabla\left[k_t(T)\nabla T\right] + H(x, y, z) = \rho C_p \frac{\partial T}{\partial T} \qquad (1)$$

where T(x, y, z, t) is temperature function and H(x, y, z, t) is heat generation rate per unit volume; ρ is density of solid; Cp is specific heat and k_t is thermal conductivity.

This differential equation is discretized when a physical process is simulated with a conventional numerical method. This is not the case with TLM method, which is intrinsically a

discrete approach that models a physical process directly. Its algorithm preserves physical significance of phenomenon under investigation [2].

It is known that a pulse on a transmission line obeys Maxwell's curl equations for propagation in a lossy medium, which leads to the telegrapher's equation [4]:

$$\nabla^2\Phi = 2\alpha\, R_d C_d \frac{\partial\Phi}{\partial t} + \alpha\, L_d C_d \frac{\partial^2\Phi}{\partial t^2} \qquad (2)$$

where $\Phi(x, y, z, t)$ is potential and L_d, C_d and R_d are inductance, capacitance, and resistance per unit of length, respectively. Constant $\alpha = 1$, 2 or 3 for one, two and three dimensions. Equation (2) is without loss if $R_d=0$ and becomes consequently identical to a wave equation. On the other hand, if $R_d\neq0$, then the equation describes an attenuated wave. When the first time-derived term on the right-hand side of equation (2) dominates the second time-derived term, one can establish equivalence with the thermal diffusion process described by equation (1). Hence, one practical application of the TLM method is its use to model physical problems where electrical/thermal analogies are possible.

The TLM method operates on a grid structure and replaces each node with an equivalent circuit of transmission lines. An equivalent TLM node of the structure under investigation is shown in Fig.1. When a pulse is sent on a transmission line element, the potential F obeys the telegrapher's equation (2). In the TLM, data in the form of potential or current values are represented by delta pulses. It is also supposed that all these pulses move in the network in synchronism. In Fig.1, the current generator I is used to model the generation of heat within the device. It represents the power injected in each node (x, y, z) in the active area. Electrical resistance and localized capacitance, in a transmission line without loss, model thermal resistance and heat capacity of the material, respectively. They are given by the following equations:

$$R_X = \frac{dx}{2K_t dydz} \quad , R_Y = \frac{dy}{2K_t dxdz} \quad , R_Z = \frac{dz}{2K_t dydx}$$
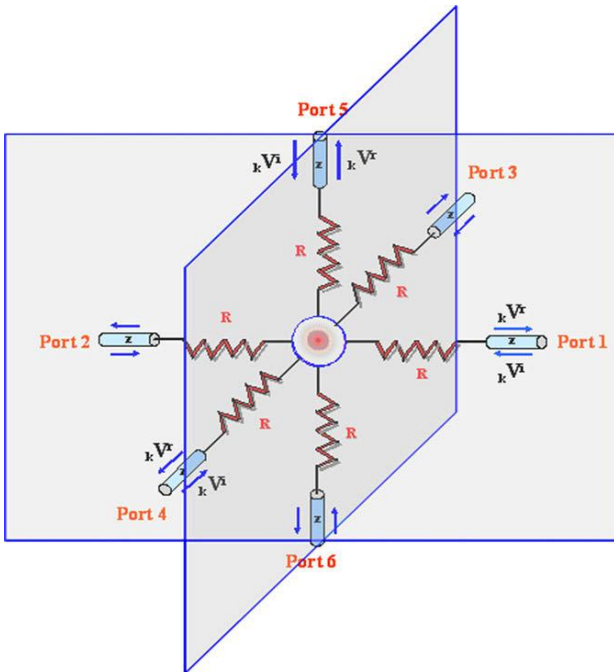$$Z = \frac{\alpha\,\Delta t}{\rho C_p \Delta x \Delta y \Delta z} \qquad (3)$$

Fig.1. A single three-dimensional TLM node.

An iterative method is used to obtain nodal potential (temperature) resulting from the injection of delta pulses (input heat) in the network after each time step. Indeed, when pulses travel down the transmission lines, they are scattered at nodes, with part of pulse reflected into the same line and the other part transmitted to neighboring nodes. Hence, local nodes potentials provide an exact solution to equation (2) at each time step. Directions of pulses on each numbered port are shown on Fig.1. These pulses are labeled $_kV_j^{i,r}$ with j indicating the direction and k the kth iteration.

Applying Thevenin and Millman theorems to equivalent electric circuit of a TLM node, nodal potential V at the kth iteration can be derived:

$$_kV = \left[\frac{2\left(_kV_1^i + _kV_2^i\right)}{R_X + Z} + \frac{2\left(_kV_3^i + _kV_4^i\right)}{R_Y + Z} + \frac{2\left(_kV_5^i + _kV_6^i\right)}{R_Z + Z} + I\right]\frac{1}{Y}$$
$$Y = \frac{1}{\dfrac{1}{R_X + Z} + \dfrac{1}{R_Y + Z} + \dfrac{1}{R_Z + Z}} \qquad (4)\text{ICLE}$$

where $Z=3\Delta t/C$ is the characteristic impedance.

Reflected pulses at a node, indicated by superscript r, are calculated according to:

$$_kV_{1,2}^r = \frac{Z\,_kV + \left(R_X - Z\right)_kV_{1,2}^i}{R_X + Z},$$
$$_kV_{3,4}^r = \frac{Z\,_kV + \left(R_y - Z\right)_kV_{3,4}^i}{R_y + Z}, \qquad (5)$$
$$_kV_{5,6}^r = \frac{Z\,_kV + \left(R_z - Z\right)_kV_{5,6}^i}{R_z + Z}$$

Each pulse takes a time Δt to move down a transmission line joining two neighboring nodes. Reflections at discontinuities, due to impedance mismatch, give incident pulses at (k+1)th iteration:

$$_{k+1}V_j^i(x, y, z) = \Gamma_j(x, y, z)_kV_j^r(x, y, z) +$$
$$\left[1 - \Gamma_j(u, v, w)\right]_kV_{j'}^r(u, v, w) \qquad (6)$$
$$with \quad \Gamma_j = \frac{Z(u, v, w) - Z(x, y, z)}{Z(u, v, w) + Z(x, y, z)}$$

Table 1 shows j, j', u, v and w values.

j	j'	u	v	w
1	2	x-1	y	z
2	1	x+1	y	z
3	4	x	y-1	z
4	3	x	y+1	z
5	6	x	y	z-1
6	5	x	y	z+1

Table 1 : j, j', u, v and w values.

Implementation of a TLM routine consists solely of repeated application of equations (4)–(6). TLM simulation algorithm can be accelerated by timestep changes and grid coarsening.
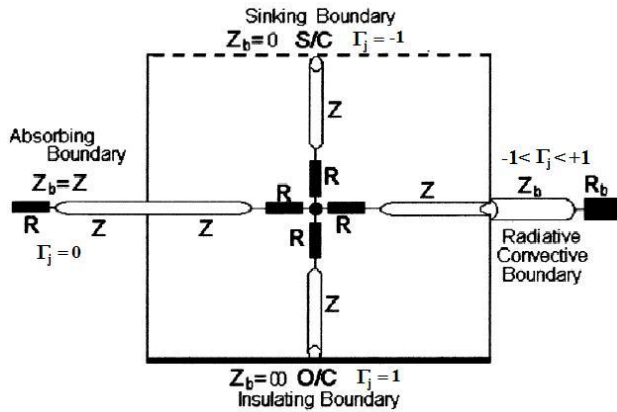
Fig.2 TLM boundary conditions.

Boundary conditions express interaction of system at hand with its surroundings. Boundaries are part of the transport model and thus should be consistent with the description of heat transport inside the medium. A heat sinking boundary corresponds to an electrical short-circuit (S/C) and Γ_j = -1, thus any incident pulse on the boundary will be returned equal in magnitude but reversed phase. A heat insulating boundary corresponds to an electrical open-circuit (O/C) and Γ_j = 1, thus any incident pulse on the boundary will be returned equal in magnitude and in phase. A symmetry boundary is represented by an electrical open-circuit in TLM modeling [2,4]. Convective or radiative heat losses at boundaries may be considered as a heat sink and modeled using an appropriate reflection coefficient, Fig.2. A constant heat source boundary, Φ_b, is modeled by taking, at the boundary interface:

$$V_b^i + V_b^r = \Phi_b$$

where V_b^i and V_b^r are incident and reflected pulses of the node attached to the source at the surface.

3. Self-heating in AlGaN/GaN power transistors

Gallium nitride (GaN) and its compounds are being established as materials of extreme significance for next generation high-density power devices. Due to their high breakdown voltages, high electron mobility, and high thermal conductivities, these materials allow the fabrication of devices, which can operate at voltages, and temperature ranges beyond the conventional semiconductor materials, such as GaAs and Si. They are used in microwave radar and mobile telecommunications [10,11]. AlGaN/GaN heterostructure field-effect transistors symbolized by HFET, operate at high frequency with a high signal-to-noise ratio. However, operation of these devices is limited by self-heating under pulsed working conditions and other problems associated with high densities of defects. This self-heating makes thermal management a crucial aspect in device-packaging design. Several system-level cooling schemes have been presented for efficient heat dissipation, such as flip-chip bonding, two-phase spray cooling and mounting devices onto high thermal conductivity substrates [12–16].
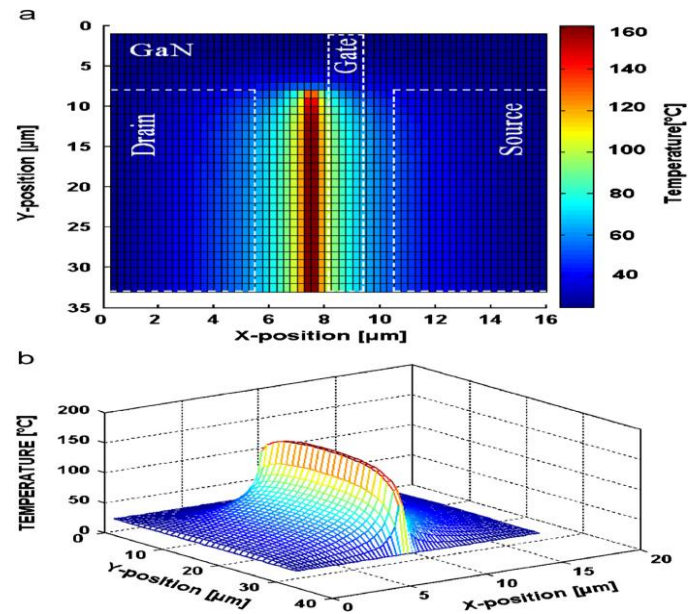

Fig.3 Temperature distribution around active region.

Fig.3a shows the surface temperature of GaN that contains the active zone. A hot-area with a maximum temperature of approximately 160.7°C, located between the source and the drain meadows of the HFET gate, is clearly visible. Fig.3b is a 3D representation of the same surface. It shows a dorsal-like temperature distribution with a peak value near the drain because of the dissymmetry. With this representation of TLM results, one can easily evaluate temperature at each point of device. This represents a great advantage compared with certain measurement techniques such as, infrared (IR) thermography or micro-Raman spectroscopy, where the temperature-measured value is an average taken at a certain thickness of device.
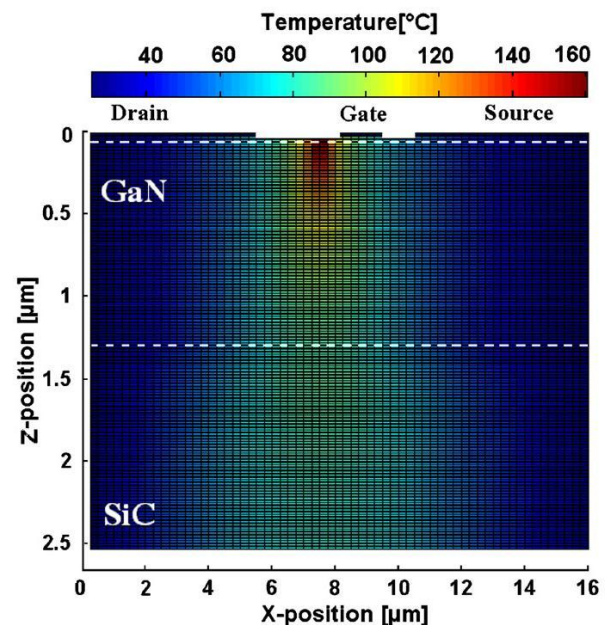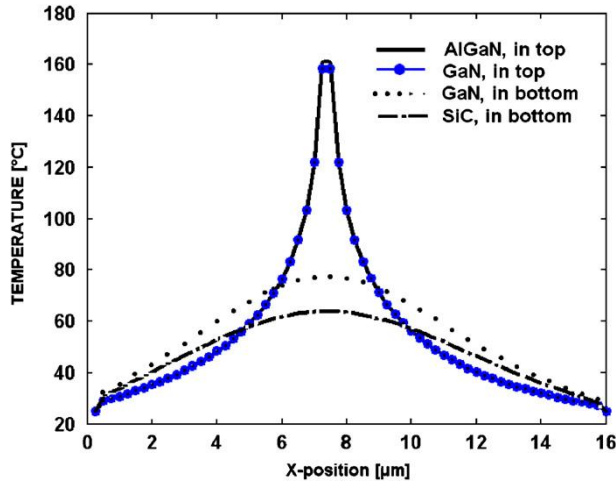

Fig.4 Temperature distribution along the z-axis.

Fig.5 Temperature distribution at various depth levels.

Fig.4 shows temperature distribution along the z-axis and Fig.5 shows temperature distribution along the x-axis at four interface positions: AlGaN layer, AlGaN/GaN, GaN/SiC and SiC/sink. This vertical cut through different device layers gives in-depth information on heat management in each layer. Furthermore, change in slope indicates a change in heat transfer dynamics going from a layer to another. Temperature in the AlGaN layer of the device is higher than that found in the GaN layer [17,18]. But heat does not accumulate at various interfaces, which otherwise would be a problem since it might lead to hot-spot formation. Hence, in comparison with other analysis methods, with TLM one can determine the place and form of hot area with more precision.

4. Electro-thermal analysis of IGBT modules.

Trends in power converter systems are to reduce converter size and to increase switching frequency. Both requirements increase heat generation rates which become a critical issue to study and optimize. This is the case of insulated gate bipolar transistor **(IGBT)** modules with their high voltage (several kV) and high current (several kA). Here, a thermal analysis of a 1200 A, 3.3 kV IGBT module was investigated and analyzed using Three-Dimensional Transmission Line Matrix (3D-TLM), Fig.6, including measurement and numerical results obtained by other simulators tools as MSC.PATRAN [19], FLOTHERM [20] and LAASTHERM [21]. Thermal simulations were run for various power loads and devices with different heat spreaders such as AlSiC, Cu–Mo, Graphite–Cu and Cu of various thicknesses.

IGBT modules have exhibited different thermal behaviors depending on substrate material used. Materials such as Aluminium Nitride (AlN), Diamond and BeO have particularly good thermal conductivity. These ceramics provide electrical insulation to the underlying base plate, which is usually pressure mounted onto a heat sink by peripheral bolts [22]. The use of ceramic substrates is to decrease self-heating from heat sources localized within IGBT modules.
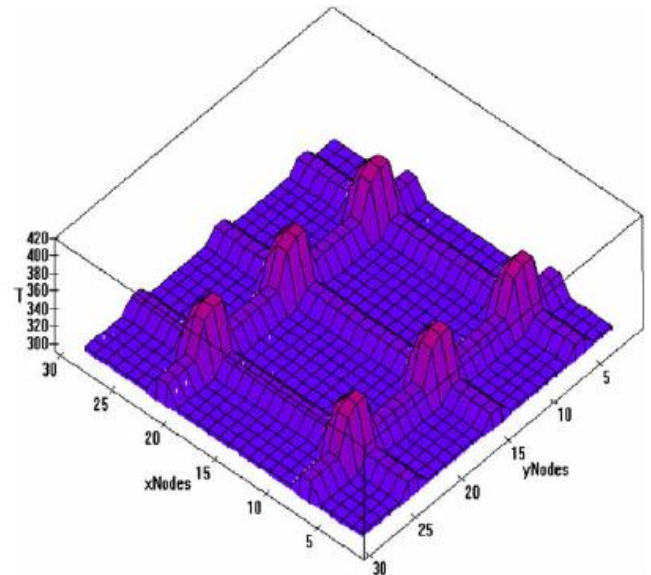

Fig.6 Typical TLM temperature distribution in an IGBT module.

Prediction of temperature rise is important in pulse operation conditions, Fig.7. This temperature profile is obtained with 100 W-step pulses where control signals are generated via a PWM scheme. Temperature rises are calculated using TLM for three load cycles and result is shown in Fig.8. During first load cycle, temperature rise and drop are important, and then thermal gradient decrease with increasing load cycles. Other simulations were performed to show the importance of heat spreaders that are included between the device and its heat sink. Fig.9 shows results for three heat spreaders AlSiC, Cu and CuMo. Thermal transients cross-over occurs at different points in time. The main difference between Cu and CuMo in terms of thermal properties is that Cu has a significantly higher thermal conductivity K, and a higher thermal diffusivity than CuMo.
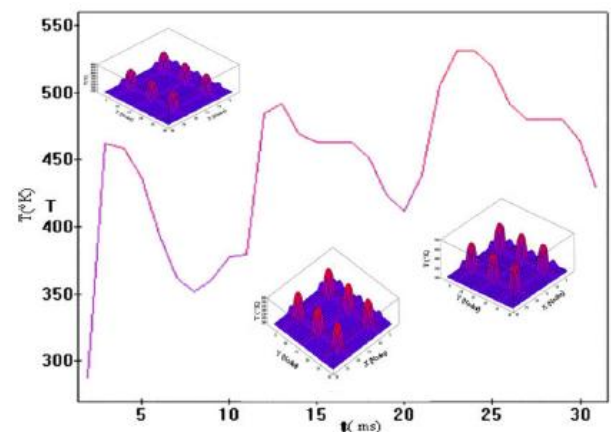

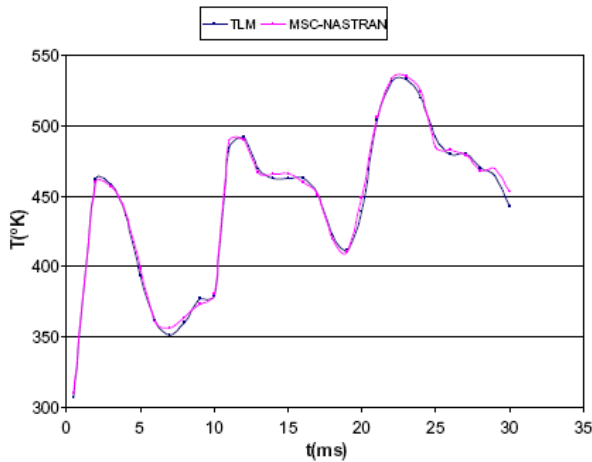Fig.7 Temperature evolution in pulsed mode.
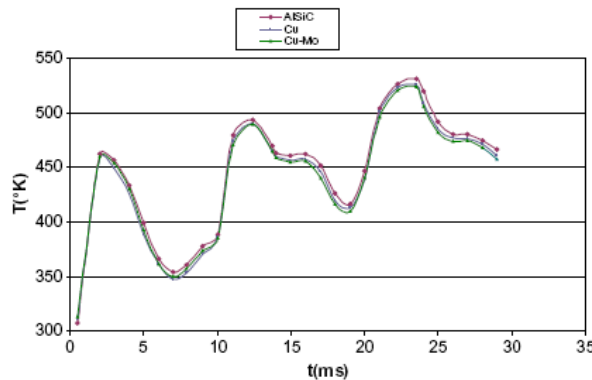
Fig.8 Comparison of TLM and MSC-NASTRAN.

Fig.9 TLM results for 3 different heat spreaders.

Temperature differences are larger in the case of AlSiC spreader, which is associated with higher chip and solder temperatures. Although thermal diffusivity of AlSiC falls between that of Cu and that of CuMo, and its thermal conductivity is less than a half of that of Cu and its specific heat capacity - density product is only a third that of CuMo, chip temperatures were found to be lowest with a Cu spreader and highest with an AlSiC spreader with CuMo yielding intermediate values. This means that the model with the CuMo heat spreader always starts each successive pulse at a lower temperature than the model with a Cu heat spreader. Since the assembly is a layered structure, materials with different CTE can cause the layers of the assembly to warp when subjected to rapid thermal excitation. Therefore, component design should not only take into account thermal and physical problems inherent to chip-to-heat sink assembly, but also interaction issues between layers of heat sink assembly itself. This implies that, as the number of pulses increases, cooling rates of heat sink assembly will play a more important role in ensuring an acceptable overall temperature, as relatively more heat will be dissipated with each successive pulse.

5. Conclusion

The TLM method was applied to study self-heating in AlGaN/GaN device structures and insulated gate bipolar transistor (IGBT) modules. The method is easy to program and gives insights on temperature distribution throughout the device. It allows a better understanding of heat behavior and management at each layer that forms the structure. Absolute

temperature determination and precise hot-area size knowledge are very difficult to assess in both HFET devices employing IR micro-thermography or in IGBT interfaces. The TLM can be a good alternative design tool, since it allows the evaluation of temperature at any point of the structure. Its physical resolution depends on the grid used only and complex geometries can be dealt with easily. Some TLM simulations results have been compared with those obtained experimentally using integrated micro-Raman/IR thermography methods or with other modeling methods, and have been found to agree within the bounds set by the resolution required. TLM method will prove handy in the study of heat management of many materials used in semiconductor devices fabrication. TLM has also the advantage upon other numerical methods of being unconditionally stable, one step, can adapt to complex geometries, and simple to program.

References

[1] P.B. Johns, R.L. Beurle, Proceedings of the IEE 118 (1971) 1203.

[2] D. de Cogan, W.J. O'Connor, S. Pulko, Transmission Line Matrix Modelling in Computational Mechanics, Taylor & Francis, CRC Press, London, 2006.

[3] C. Christopoulos, The Transmission-Line Modeling Method (TLM), IEEE Press, New York, 1995.

[4] D. De Cogan, Transmission Line Matrix (TLM) Techniques for Diffusion Applications, Gordon and Breach, 1998.

[5] A. Saleh, P. Blanchfield, , International Journal of Numerical Modeling, 3 (1990) 39.

[6] I.J.G. Scott, D. de Cogan, Journal of Sound and Vibration , 311 (2008) 1213.

[7] A.Amri, A.Saidane, S.Pulko, Computers in Biology & Medicine 41 (2011) 76.

[8] S.Aliouat-Bellia, A.Saidane, A.Hamou, M.Benzohra, J.M.Saiter, Burns 34 (2008) 688.

[9] W.J.R. Hoefer, The transmission line matrix (TLM) method, in: T. Itoh (Ed.), Numerical Techniques for Microwave and Millimeter-Wave Passive Structures, Wiley, 1989.

[9] A.K. Iyer, G.V. Eleftheriades, Applied Physics Letters 92 (2008) 131.

[10] S. Nuttinck, E. Gebara, J. Laskar, M. Harris, IEEE Microw. Mag. 3/1 (2002) 80.

[11] M. Kuzuhara, H. Miyamoto, Y. Ando, T. Inoue, Y. Okamoto, T. Nakayama, Phys. Stat. Sol. A 200/1 (2003) 161.

[12] J.J. Xu, Y.F. Wu, S. Keller, G. Parish, S. Heikman, B.J. Thibeault, U.K. Mishra, R.A. York, IEEE Microw. Guided Wave Lett. 9/7 (1999) 277.

[13] J. Sun, H. Fatima, A. Koudymov, A. Chitnis, X. Hu, H.M. Wang, J. Zhang, G. Simin, J. Yang, M.A. Khan, IEEE Electron. Device Lett. 24/4 (1999) 375.

[14] S.L. Lee, Z.H. Yang, Y. Hsyua, J. Heat Transf. 116 (1994) 167.

[15] S .Heffington, W.Z. Black, A. Glezer., in: Proceedings of International Electronic Packaging Conference, (2001) 779.

[16] J.Y Murthy, C.H Amon, K. Gabriel, P. Kumta, S.C. Yao, . , in: Proceedings of International Electronic Packaging Conference, (2001) 733.

[17] S. Rajasingam, J.W. Pomeroy, M. Kuball, M.J. Uren, T. Martin, D.C. Herbert, K.P. Hilton, R.S. Balmer, IEEE Electron. Device Lett. 25 (7) (2004) 456.

[18] I. Ahmad, V. Kasisomayajula, M. Holtz, J.M. Berg, S.R. Kurtz, C.P. Tigges, A.A. Allerman, A.G. Baca, Appl. Phys. Lett. 86 (17) (2005) 503.

[19] MSC.PATRAN, complete software environment for simulation, (http://www.mscsoftware.com.au/).

[20] ANSYS FLOTHERM, Ansys Inc, (http://www.ansys.com).

[21] A. Hamidi, G. Coquerz, R. Lallemand, P. Vales, Microelectron. Reliability J., 38 (1998) 1353.

[22] C.Van Godbold,V. Sankaran, J.L. Hudgins, IEEE Trans. Power Electron. , 12 /1 (1997) 3

Simulation of a photovoltaic pumping system using the flux oriented control

A. Meflah[a] and T. Allaoui[b]

[a]Department of physic, University of Abou-bakr Belkaid Research Unit Materials and Renewable Energy,Tlemcen,Algeria,
[b] Electrical Engineering Laboratories, Department of Science and Technology University Ibn Khaldoun,
Zaarouea,Tiaret,Algeria,

Abstract

   The objective of this Work is to provide a vector control combined with an electric asynchronous motor. The configuration of this system includes a photovoltaic generator (PVG), a PV bus, a PV filter connected to a boost converter, a DC bus and a voltage inverter fed induction machine coupled to a centrifugal pump. To ensure operation at maximum power of PV system for various climatic conditions, the MPPT (Maximum power point tracking) control is used. At the end of control flow and total head of pumping station, the control strategy for flux vector oriented FOC (flux oriented control) served here as a solution. Simulation results show the effectiveness of different commands used in this system.

Key words: Photovoltaic; MPPT; flux oriented control; asynchronous machine.

1. Introduction

   Since the widespread use of electricity, energy consumption has been increasing, the problem of conversion and energy storage has led to research and develop new sources of supply. PV pumping system usually consists of a PV generator, a power converter, motor and pump. The asynchronous machine occupies a very important industry and transport. It is valued for its strength, low purchase price and maintenance. The order is against more difficult than for other electrical machines [1]. It has not been immediately a boom since the regulations at the time, based on analogue components; the implementation of the order was difficult. We begin by modeling of the global system. Next, we explain the principle of FOC. Finally, simulation results based closed loop are presented to illustrate the validity and performance of the control study.

2. Modeling of the global system

   The pumping system is the combination of a set of interconnected subsystems that are the PV array, the chopper adapter impedance (MPPT), the voltage inverter, the cage induction motor and centrifugal pump associated with a discharge line. Figure 1 the schematic block diagram of such a system.
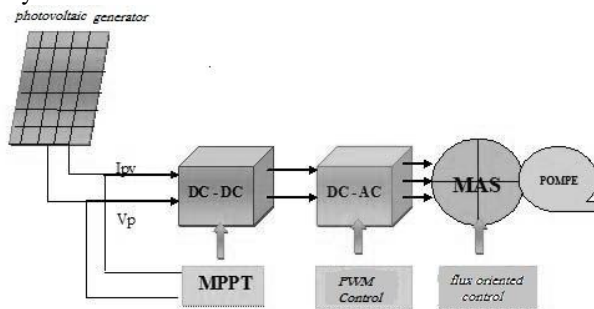

Figure.1   System overview.

2.1 Model of the Photovoltaic generator

   The PVG has a current/voltage characteristic strongly nonlinear as a direct result of the behavior of semiconductor junctions that are the basis for its implementation. Studies conducted by specialists in various fields of application have led to the development of many models of generators. PVG is a made up of N_{bp} branches in parallel and each branch consists of modules in series with N_{ms} in turn N_{cs} cells in series [2].

   The operation of this generator is modeled by the following approximate analytical expression:

$$I_p = N_{bp} \left[I_{ph} - I_s \left(e^{\frac{V_p}{V_T\, N_{cs} N_{ms}}} - 1 \right) \right] \qquad (1)$$

$$I_{ph} = q\, g\, (L_n + L_p) \qquad (2)$$

$$V_T = \frac{n\, K_B\, T}{q} \qquad (3)$$

I_{ph}: Stock photo of a cell (A).
E: global solar irradiance (W/m2).
I_s: the saturation current of the diode (A).
V_T: thermodynamic potential of a cell (V).
I_p: Current supplied by the PVG (A).
L_n: electron diffusion length (m).
L_P: diffusion length of holes (m).
g: generation-recombination rate (m3/s).
Vp: the output voltage across the PVG (V).
n: ideality factor of the solar cell.

   The PV array used in this system is the «Shell SP75» consists of eight modules, with their characteristics are listed in Tables II, II and III

2.2 Maximum power point tracking MPPT

Several MPPT algorithms have been proposed in the literature, including P&O (perturbation and observation), the method of load voltage, the method of short-circuit, the incremental conductance algorithm and the method of the network of artificial neural. The algorithm MPPT P&O is the most commonly used in commercial products PV [3]. P&O algorithm is detailed in Figure 2.
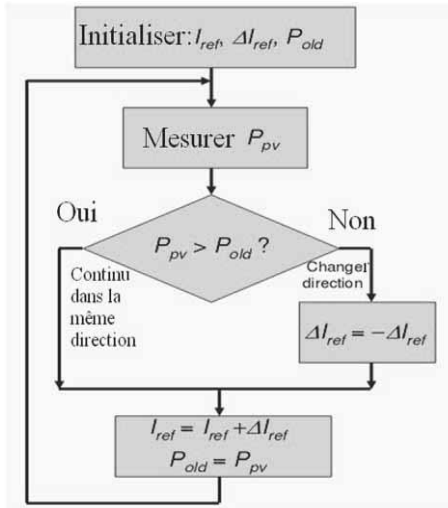
Figure.2   The P&O MPPT algorithm.

2.3 Model of the inverter

The three-phase inverter PWM (pulses with modulation) consists of three independent arms, each includes two switches. Each switch consists of a transistor (IGBT, MOSFET ...) and a diode connected in antiparallel. To avoid subjecting the output of the PVG to overvoltage from the inverter is inserted between the two capacitors [4].

The voltage across the capacitor is equal to Vp, the current ic is expressed as:

$$i_c = C \cdot \frac{d\, v_p}{dt} \qquad (4)$$

$$i_c = i_p - i_{eo} \qquad (5)$$

The relation which connects the input current and output current of the inverter is given by the following expression:

$$i_{eo} = i_a C_1 + i_b C_2 + i_c C_3 \qquad (6)$$

The switches of each arm of the inverter are complementary; it is the same for the associated control signals. We can write:

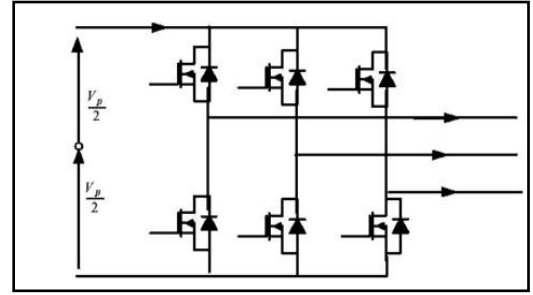$$C_4 = 1 - C_1 \quad C_5 = 1 - C_2 \quad C_6 = 1 - C_3 \qquad (7)$$

Figure.3   Voltage PWM Inverter.

3. Flux oriented control.

The principle of this control is to reduce the electromagnetic torque equation of the machine in order to be comparable to that of a DC machine.

The transient torque is expressed in the reference d, q as a cross product of currents or streams:

$$C_e = p \frac{M}{L_r} (\varphi_{dr} i_{qs} - \varphi_{qr} i_{ds}) \qquad (8)$$

We see that if one eliminates the second product (φ_{qr}, i_{ds}), while the couple looked very much like that of a DC machine. It is sufficient to do so, direct the d_q reference so as to cancel the component of flux in quadrature. That is to say, to choose the proper rotation angle Park so that the rotor flux is entirely focused on the direct axis (d) and therefore have $\varphi_{qr} = 0$. Thus $\varphi_r = \varphi_{qr}$ only (Figure 4).
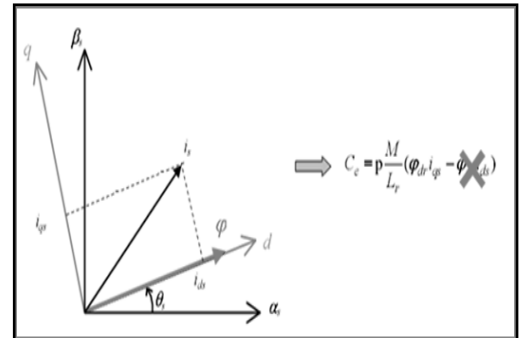
Figure.4   Principle of Vector Control.

The couple is then:

$$C_e = p \frac{M}{L_r} \varphi_r i_{qs} \qquad (9)$$

It should regulate the flow by acting on the component of the stator current ids and it regulates the torque acting on the component i_{qs}. Figure 3 summarizes this regulation because it shows a diagram of vector control of induction motor with speed control and regulation of the two currents ids and i_{qs}. We then have two action variables as in the case of DC machine. One strategy is to let the constant component ids. That is to say, to fix its reference so as to impose a nominal flux in the machine. The current controller handles i_{ds}* to maintain the current ids constant and equal to the reference

$i_{ds}*$ ($i_{ds} = i_{ds}$ Reference). If you want to speed up the machine, thus increasing its speed, it requires a reference current $i_{qs}*$ positive. The current controller i_{qs} will impose the reference current to the machine [5]. The Figure 6 shows the Bloc of flux oriented control in SIMULINK.
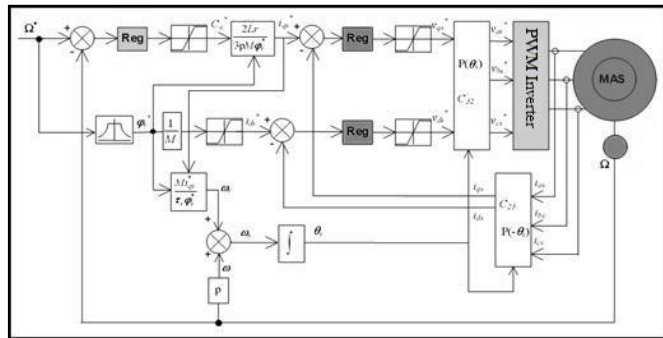

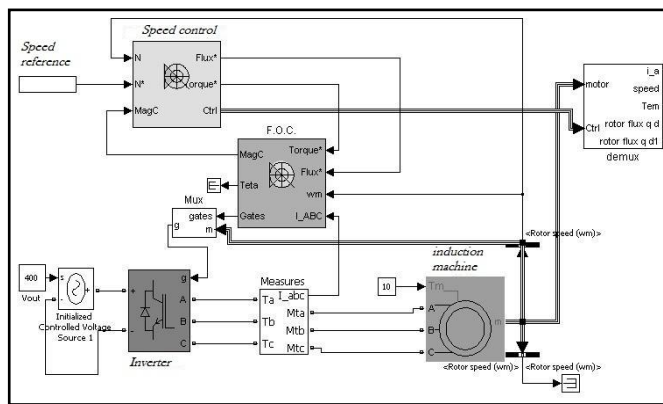Figure.5   Speed control of induction motor in FOC.

Figure.6   Bloc of flux oriented control in SIMULINK

4. Results

As part of this application, the choice of values has been fixed.

TABLE I.   ELECTRICAL CHARACTERISTICS OF PVG (SHELL SP 75.) [6]

Electrical parameters of the panel in the STC: The **illumination** E = 1000W/m², the cell temperature T = 25°C.	
Maximum peak power, P_m.	75 W
Maximum voltage, V_m.	17 V
Maximum current I_m.	4.4 A
Open circuit voltage, V_{oc}.	21.7 V
Short-circuit current, I_{sc}.	4.8 A

TABLE II.   INDUCTION MOTOR (3 HP DRIVE.)

Voltage	V = 220 V
Motor stator resistance	R_s = 0.01485 Ω
Motor rotor resistance	R_r = 0.00929 Ω
Self-inductance of a stator	L_s = 0.3027 mH
Self-inductance of rotor	L_r = 0.3027 mH
mutual inductances	L_m = 0.3027 mH
Number of pole pairs of the motor	p = 2

TABLE III.   CHARACTERISTICS OF THE CENTRIFUGAL PUMP.

Performance of the pump at a speed of 2900 rev / min:
Maximum flow: Q_{max} = 30 m³ / h. Maximum lift: H_r = 80 m. Horsepower: P_m = 14 kW.

All simulations are performed in MATLAB/SIMULINK 7.10. The results are illustrated by the following figures:
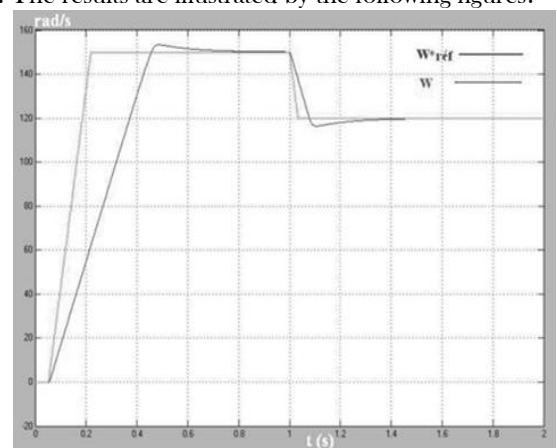

Figure.7   Rotor speed "ω" and its reference.
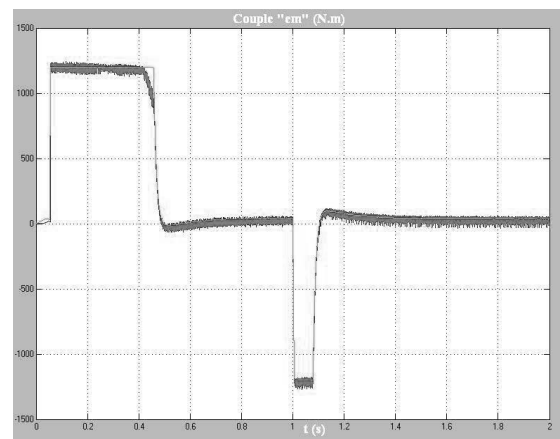

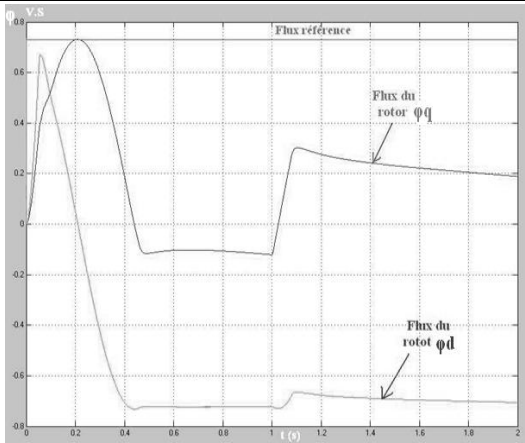Figure.8   The electromagnetic torque and its reference.

Figure.9   The quadratic and direct rotor flux.

Figure.10   The pump flow Q (t).

In Figure 7, the speed of the machine follows its set point without overshoot showing the effectiveness of the control loop speed. This allows then to achieve the flow and total head desired. Figure 8 and 9 shows the appearance of the couple set superimposed on the torque simulated by the model of the machine and the mechanical speed, and the decoupling between the quadratic and the direct rotor flux, the rotor flux axis d and q along the same test, we see that the q-axis flux is very small as desired and the flow axis d is set, this is proof of decoupling of the axes of the rotor flux vector control with oriented. This result reveals the effectiveness of vector control

in sudden changes in electromagnetic torque. At the last simulation of global system, the pump will reach a speed close to: $19 m^3/h$.

5. Conclusion

In this work, we studied and modelled the various components of a complex system, that of an asynchronous motor pump powered by PV generator through a chopper and an inverter. This paper shows that the model of the solar module, based on its equivalent circuit is nonlinear; in fact, it is based on the weather and its load. We chose to study the P&O algorithm to determine the source strength and its direction of variation. Since the model of the overall system is highly nonlinear, we used a robust control technique and more specifically FOC.

The simulation results showed that it is possible to adjust appropriately adapting MPPT, the stator currents and speed, regardless of the type proposed decoupling. The control strategy for flux vector oriented FOC served here as a solution to control the flow and head full of photovoltaic pumping station.

References

[1] L. Baghli, "Contribution to the Control of Asynchronous Machine, Using Fuzzy Logic, Neural Networks and Genetic Algorithms", PhD Thesis, University Henri Poincaré, Nancy, (1999).

[2] M. Simoes and F. Farret, Renewable Energy Systems, Pub. CRC Press, ISBN 0849320313, 2004.

[3] K. Chomsuwan, P. Prisuwanna, "Photovoltaic grid-connected inverter using two-switch buck boost converter," in Conf. Rec. IEEE Photovoltaic Specialists Conf 2002., Pp.. 1527-1530, May 2002.

[4] M. F. Mimouni, M. N. Mansouri, B. Benganem and Annabi, Renewable Energy, 29(3),(2004),433-442,.

[5] L. BAGHLI , IUFM Lorraine-UHP,(2005).

[6] R. Khezzar1, M. Zereg, Review of Renewable Energy. 13 (3), (2010) 379-388.

The electrochemical nucleation and properties of the Co-Cu alloys thin films deposited on FTO substrate

L. Mentar* and A. Azizi

Laboratoire de Chimie, Ingénierie Moléculaire et Nanostructures, Département de Chimie, Faculté des Sciences,
Université Ferhat Abbas- Sétif, 19000 Algérie
*menter.loubna@yahoo.fr

Abstract

In this study, the properties of Co-Cu alloys thin films prepared by the electrodeposition method from a sulfate bath under potentiostatic conditions on a fluorine-doped tin oxide (FTO)-coated conducting glass substrate have been investigated. The electrochemical characteristics of granular alloys were studied by using cyclic voltammetry (CV) and chronoamperometry (CA) techniques. The structural behaviors of the deposits have been determined by X-ray diffraction (XRD) measurements. The magnetic properties were investigated by alternating gradient force magnetometer (AGFM) technique. The effect of deposition potential on the electrodeposition process, phase structure and magnetic behaviors has been studied. CV studies revealed that the potential of Co dissolution depends on experimental parameters such as presence of Cu ions and cathodic limit. X-ray diffraction patterns of the Co-Cu alloys thin films exhibit an fcc and hcp phases, with peaks quite close to those of the Co phase (fcc and hcp). Magnetic properties such as coercivity and saturation magnetization showed strong dependence on the crystallite size and consequently the deposition potentials.

Keywords : electrodeposition; Co-Cu alloys; structure; magnetic.

1. Introduction

Systems, composed of immiscible materials such as Co-Ag or Co-Cu [1, 2] consist of small grains of the magnetic metal isolated in the non-magnetic matrix. The difference in the spin-dependent scattering for aligned and randomly oriented magnetic moment generates a giant magnetoresistance (GMR). The discovery of this phenomenon in Co-Cu systems, thin films of cobalt and copper has been investigated for basic research and applications [3]. The effect is exploited commercially by manufacturers of hard disk drives, the magnetic sensors on the reading heads of computers or some music players, etc. The granular alloy films are immiscible combinations usually prepared by physical deposition methods [1,4]. Recently, electrochemical deposition is widely used to produce multilayered alloys exhibiting giant magnetoresistance (GMR) [5-16]. This technique is preferred in low-end applications such as GMR sensors in automotive applications or in microsystems [15, 16]. The simplicity, cost effectiveness, easy scale up, and possibility to grow films on irregular surfaces make the process more versatile. The solid solubility limit of Cu in Co at room temperature is almost 0% in the equilibrium state [17]. However, the electrodeposition made the Co-Cu alloy in nonequilibrium supersaturated solid solution state. It is well known, that the nucleation-growth process, the morphology, the microstructures and magnetic properties of Co-Cu electrodeposits depend greatly on solution composition, pH, temperature, and applied potential or current density [18-27]. Several baths with different compositions have been used for electrodeposition of Co-Cu thin films. Among them the bath, with or without additives, are usually used to electrodeposite Co-Cu granular thin films. The formation of continuous film of Co-Cu alloys thin films requires a detailed understanding of the microstructure and the role of parameters such as applied potential on the properties of deposits. Consequently, the aim of this work is to study of the influence of the deposition potential in the electrochemical nucleation and the properties of the Co-Cu alloys thin films. The electrochemical behaviour and composition of the deposited alloys were analyzed as a function of the applied potential. X-ray diffraction (XRD) and alternating gradient force magnetometer (AGFM) analysis were carried out on some deposits obtained potentiostatically.

2. Experimental Details

Co-Cu thin films were prepared by electrodeposition onto polycrystalline fluorine-doped tin oxide (FTO)-coated conducting glass substrate with an exposed area of 1×2 cm² $(10-20 \ \Omega/cm²$ sheet resistance). All the depositions were made in a three-electrode cell containing Pt as a counter electrode, saturated calomel electrode (SCE) as reference and FTO coated glass as a working electrode. The FTO substrate was first degreased in acetone and ethanol by ultrasonication for 15 min, and lastly well rinsed with distilled water. The thin films alloys were deposited in a potentiostatic mode, using a computer controlled potentiostat/galvanostat (Voltalab 40) as a potential source. The electrolyte contained 0.25M cobalt sulfate, 0.005 M copper sulfate, 1M sodium sulfate, and 0.5M boric acid, pH was adjusted to 3.8 using diluted H_2SO_4. Electrodeposition was performed at room temperature, without stirring. The structural characterization was performed by XRD through θ-2θ scans using a Siemens D5000 diffractometer equipped with a monochromatic Cu source ($\lambda CuK\alpha_1 = 0.154056$ nm). The magnetic measurements were performed with an alternating gradient force magnetometer (AGFM) at room temperature.

3. Results

To define the major characteristics of the Cu, Co and Co-Cu alloy deposition process, the cyclic voltammetry technique was used. Typical CVs of FTO electrode recorded in (a) 0.25

M $CoSO_4$ and (b) 0.25 M $CoSO_4$ + 0.005 M Cu SO_4 solutions are shown in Fig. 1. On the forward scan, the voltammograms show an abrupt increase in current at a potential of approximately –1.03 V vs. SCE which is the starting point of the reduction of the Co species. Fig. 1a also shows that dissolution of the deposits starts at around 0.0 V on the reverse scan, in agreement with previous studies on the electrochemical deposition of Co^{2+} onto FTO electrodes in sulfate aqueous solutions [28]. Figure 1b shows the CV of the 0.25 M $CoSO_4$ + 0.005 M $CuSO_4$ solution. In the direct scan, the beginning of the current decrease was detected at -0.14 V vs. SCE, which is characteristic of the overpotential deposition process of Cu onto FTO surfaces [29]. After this of Cu onto FTO, the Co deposition on Cu surface starts at around -0.89 V vs. SCE. In this case, the Co deposition potential value shifts anodic than that Co free solution. It's well established that the over-potential of metal deposition on foreign substrate is high than deposition on metal substrate. In effect, in the negative scan, Co deposited on Cu deposits instead of the FTO surface because Cu deposited at much lower negative potential than Co and the electrode surface was covered by Cu deposits before Co deposited. Since Co and Cu have very similar crystallographic structure, lower energy is required by Co to nucleate on Cu [30]. Therefore, the nucleation potential of Co shifted positive slightly, from –1.03 to -0.89 V vs.SCE, in the presence of Cu ions. On the reverse scan at -1.3 V; an intense anodic peak are observed comparable to that observed during the Co dissolution (Fig. 1a). This intense peak corresponds to Co-rich phases. Since Co and Cu could form alloy or intermetallic compounds from Co-Cu phase diagram, this peak attributed to Co-Cu phase is very rich in Co due to the very lower Cu^{2+} concentration in solution. This behavior is in agreement with the literature [30, 31]. In addition, the increase or decrease of dissolution peaks can be related to the composition of the dissolved deposit. On the other hand, the presence a crossover occurred between the cathodic and anodic current branches is the sign of a nucleation and growth process [31].
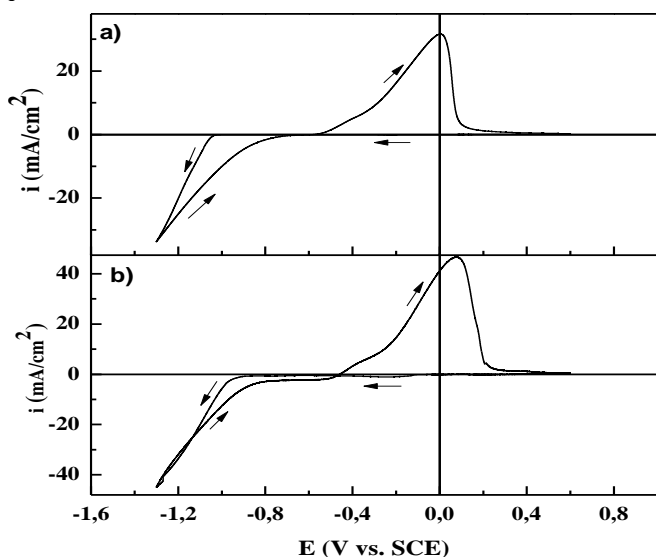
values were chosen to be within the zone where the reduction processes are observed in the voltammograms. The number of anodic peaks is related to the switching potentials. Effectively, only one peak A_2 is observed at -0.7 and -0.9 V vs. SCE. The position of this peak is related to dissolution of copper [29]. Moreover at -1.0 and -1.1 V vs. SCE, two anodic peaks A_1 and A_2 are observed. By comparing this cyclic voltammetric curves with of the oxidation of pure cobalt shown in Fig. 1a, it could be concluded that peak A_1 corresponding to the cobalt oxidation. At higher applied potential, -1.2 and -1.3 V, only one higher peak is observed (A_3), which could be attributed to Co-Cu phase very rich in Co. this can be related to decrease in copper (II) ions concentration in the solution.

In all cases, the anodic peaks shifted slightly in the positive direction. The cathodic and anodic current density increased with increasing value of switching potential, which indicated that more Co deposits were obtained in the cathodic region with a higher negative applied potential. Adjustment of the applied current led to the preparation of Co-Cu films with variable metal percentages. It was also found (see Fig. 2) that the ratio of the peak area A_1 to total anodic peak became smaller when higher negative switching potential was applied, which indicated that the copper percentage in the deposits was reduced with the higher negative electrodeposition potential applied. These results corroborate the voltammetric deposition curves, (Fig. 2b), i.e., these curves were similar to those obtained in the literature [32, 35]. The increase in polarization with increasing Co concentration in Co-Cu deposits is reported in these references. Also, this is confirmed by elemental composition of granular alloys deposited at different applied potential realized using the atomic absorption spectroscopy (AAS) measurements (not shown).
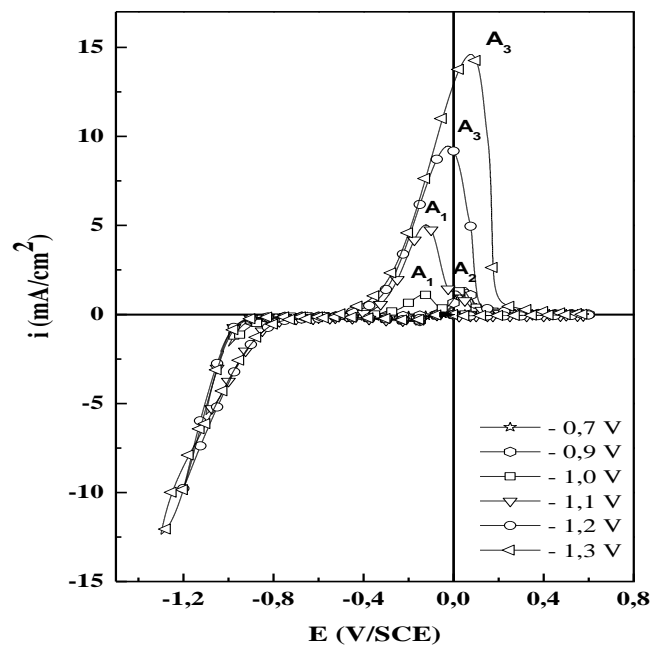

Figure 1 Cyclic voltammogram of FTO substrate in (a) 0.25 M $CoSO_4.7H_2O$ and (b) 0.25 M $CoSO_4.7H_2O$ + 0.005 M $CuSO_4.7H_2O$ with 1 M Na_2SO_4 and 0.5 M H_3BO_3 (pH=3.8) solutions. v= 20 mVs⁻¹.

Figure 2 Voltammetric curves of Co-Cu alloy deposition and dissolution from electrolytic solution 0.25 M $CoSO_4.7H_2O$ + 0.005 M $CuSO_4.7H_2O$ and 1 M Na_2SO_4 and 0.5 M H_3BO_3 (pH=3.8) solutions with six different cathodic sweep reversal potentials: from -0.7 V to -1.3 V; v = 20 mV s⁻¹

To confirm the precedent cyclic voltammetry study, the Figure 2 presents the voltammograms obtained from a solution with Co and Cu ions at different switching potentials (E_λ). E_λ

The nucleation kinetics and growth of Co-Cu onto FTO surface was studied with the chronoamperometry technique. This technique is frequently used to determine the mechanisms by which new phases are formed. The formation

of stable nuclei and their growth can be observed by monitoring the current and information on the rate of nucleation, the density of nuclei and the mechanism of growth can be obtained from the shape of the resulting current–time transient plots [29]. An example of current transients obtained at different potentials during Co-Cu electrodeposition on FTO coated glass substrates are shown in Fig. 3. It can be seen that all the curves have a characteristic peak corresponding to the nucleation of Co-Cu alloy on FTO substrate. For longer deposition time, the current density also exhibits an asymptotically decaying behavior after reaching its maximum. This asymptotic behavior of the current densities indicates a nucleation followed by diffusion controlled growth. Moreover, it is found that the current density reaches the maximum value more rapidly with increasing the potential and also increases monotonically with the potential.
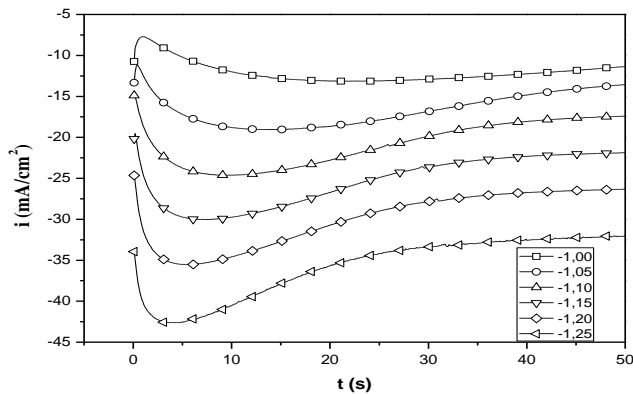

Figure 3 Current transients for Co-Cu electrodeposition on FTO-coated conducting glass substrates at the indicated final potentials.

These features are qualitatively consistent with the theoretical 3D nucleation followed by diffusion controlled growth model suggested by Scharifker and Hills [33, 34]. According to this model, the nucleation is classified into two modes: the instantaneous nucleation and the progressive nucleation modes. In instantaneous nucleation mode, all reaction sites of the surface are activated simultaneously and the number of nuclei growing on the surface is saturated at the initial deposition stage. On the other hand, in progressive nucleation mode, the number of nuclei formed on the surface is less than the maximum saturation value and new nuclei begins to grow, progressively.

In order to distinguish between instantaneous and progressive nucleation process, experimental chronoamperometric data are used by representing in a nondimensional plot $\left(\dfrac{i}{i_{max}}\right)^2$ versus $\left(\dfrac{t}{t_{max}}\right)$ and to compare these with the theoretical plots resulting from the following equations:

-for instantaneous nucleation followed by three-dimensional diffusion-limited growth is:

$$\frac{i^2}{i_{max}^2} = \frac{1.9542}{t/t_{max}}\left\{1 - exp\left[-1.2564\left(t/t_{max}\right)\right]\right\}^2 \qquad (1)$$

- and for progressive nucleation followed by three-dimensional diffusion-limited growth is:

$$\frac{i^2}{i_{max}^2} = \frac{1.2254}{t/t_{max}}\left\{1 - exp\left[-2.3367\left(t/t_{max}\right)^2\right]\right\}^2 \qquad (2)$$

where i and t are the current density and time, respectively; i_{max} and t_{max} are maximums of the current transients and time, respectively. To analyze the experimental data by means of

the theoretical model, the current transients in Fig. 3 are replaced with reduced-variable plots normalized in terms of imax and tmax. According to eqs. (1) and (2), these plots are presented in Fig. 4.
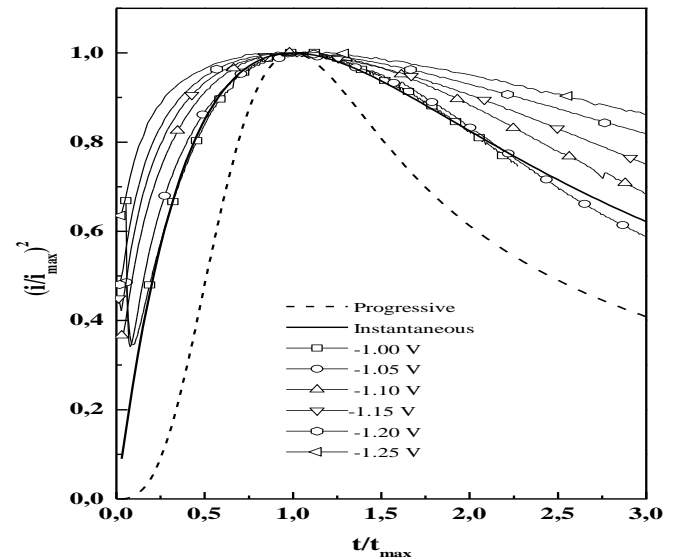

Figure 4 Normalized $\left(\dfrac{i}{i_{max}}\right)^2$ vs $\left(\dfrac{t}{t_{max}}\right)$ plots obtained from the experimental data in Fig. 3. The dotted and the solid line represent the theoretical progressive and instantaneous nucleation models, respectively.

The theoretical model curves are also shown in Fig. 4 and the solid line and the dotted line represent the theoretical plots with respect to instantaneous and progressive nucleation modes, respectively. It can be seen in the figure that all the experimental plots agree well with the instantaneous nucleation mode. This result indicates that in the initial deposition stage of Co-Cu on FTO surfaces, all the reaction sites on the surface of FTO substrate are activated simultaneously and the number of nuclei formed is saturated instantaneously.

The effect of electrodeposition potential on the phases formed in the Co–Cu thin films was analyzed using XRD. Fig. 5 shows the XRD patterns of Co-Cu thin films deposited at various applied potentials. Four peaks at 2θ values of 41.7, 44.28, 47.6 and 51.50 deg corresponding to hcp Co (100), (fcc Co (111), hcp Co(101) and fcc Co(201) planes of Co were observed, respectively. Furthermore these patterns display an fcc and hcp phase, with peaks quite close to those of the Co phase (fcc and hcp). No peaks of the Cu fcc pahse were found, which we suggest is due to the Cu clusters being too small to produce reflections [35] and only produce a distorsion of the Co lattice. It is interesting to note that such a distinct phase separation was not observed in the X-ray diffractogram studied by most of the previous researcher's [23, 25, 32] under DC deposition of Cu–Co alloys from an electrolyte without additive agent, except studies by Cohen-Hyams et al. [26]. Indeed, the annealing at high temperatures was found to improve such phase segregation in Cu–Co alloys.

From these results, it's evident that the fcc phase is dominant than the hcp phase in the Co-Cu alloy thin films. Apparently, the amount of the hcp phase increases when the applied potential decreases down to more negative value.
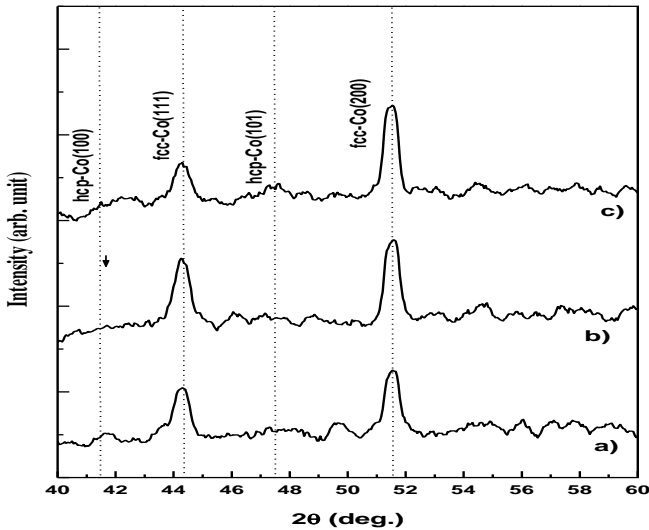
Figure 5 XRD patterns of Co-Cu thin films deposited at various applied potentials: a) – 1.1, b) -1.2 and c) -1.3 V vs. SCE, respectively.

These results are in agreement with other observations [25]. For the all granular coating of Fig. 5, the adjustment of the average cell parameters led to an '*a*' value of 0.35402 nm, this value is slightly smaller than that of pure fcc Co, 0.35446 nm (JCPDS No. 15-806), which can be explained by strains induced by the presence of Cu and fcc Co in the matrix. Under equilibrium conditions, at room temperature the Co metal exists in the hcp phase, though the fcc phase is stable above 420°C only [36]. It is known that electrochemical deposition from a bath at pH more than 2.9 results mainly in an hcp-Co [37, 38]. However, in the literature the formation of fcc-Co phase by electrodeposition at room temperature is due the presence of codischarged and dissolved hydrogen distorting the hcp lattice to an extent that it finally transformed to the fcc structure [39]. Moreover, it has been shown that when the electrolyte has pH value about 3, and in the absence of stirring, the fcc structure is favored [40]. In this case for Co-Cu electrodeposited at more negative potential, the origin for the formation of an alloy with fcc phase was due to the incorporation of a very small impurity of Cu atom in the deposit [41].

The average crystallite size along the (111) peak for fcc phases estimated from the full width at half-maximum (FWHM) values of diffraction peaks using the Scherrer formula [42],

$$D = \frac{0.9\lambda}{\beta \cos\theta}$$

(3)

where D is the crystallite size, β is the broadening of the diffraction line measured at half of its maximum intensity in radiance (FWHM), λ is the x-ray wavelength (1.5406 A°) used and θ is the diffraction angle. In table 1, the average crystallite sizes along the (111) peak for fcc phases at different values of applied potential are presented. The crystallite size was typically 20-40 nm. The alloy deposits therefore possess a nanocrystalline structure.

E (V vs. SCE)	2θ (°)	D (nm)	H$_c$ (Oe)	Ms (emu/cm^3)
-1.1	44.31	40	25.80	1868.70
-1.2	44.26	40	22.62	1408.61
-1.3	44.32	21	64.52	547.24

Table 1: The effect of deposition potential on the structural and magnetic parameters of the Co-Cu alloy thin films.

Magnetization versus magnetic field curves (M vs. H) was registered in order to analyze the magnetic response for the deposits. Fig. 6 shows the hysteresis loops of the Co-Cu films at parallel and perpendicular to the film plane at room temperature obtained at three deposition potentials, (a) -1.1, (b) -1.2 and (c) -1.3 V vs. SCE, respectively. Also, table 1 summarizes the relevant magnetic properties. These results show change in the magnetic properties, which were related to the difference in grain sizes and thickness of deposit films. Magnetic anisotropy is clearly in plane and magnetization switches by domain-wall motion. The coercivity is small (24–70 Oe) and increases greatly as applied potentials increases from -1.1 to -1.3 V vs. SCE, indicating an increase in defect density when growth is made to occur faster. This is also verified by the XRD patterns in Fig. 5, where the diffraction peaks of the film grown at -1.3 V vs. SCE are much weaker than the other ones.
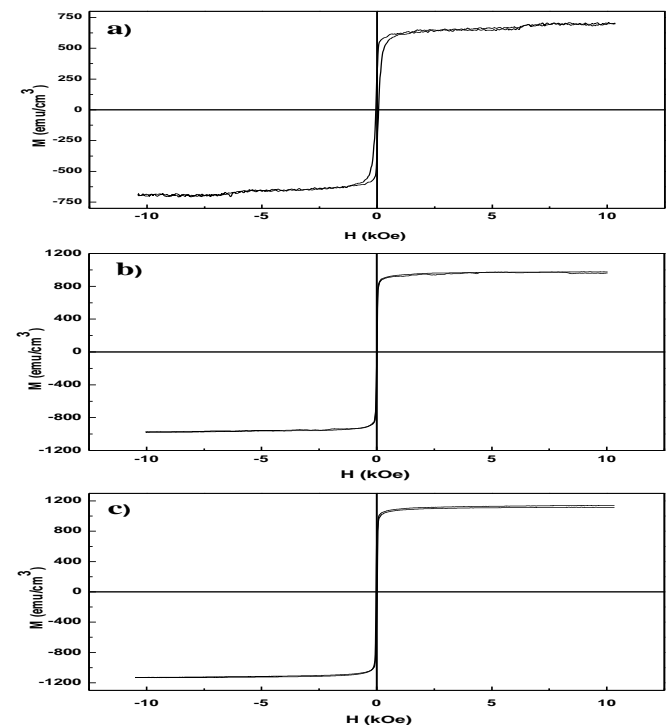

Figure 6 Hysteresis loops of Co-Cu thin films along the easy and hard magnetized orientations obtained at different applied potential: (a) -1.1, (b) -1.2 and (c) -1.3 V vs. SCE, respectively.

4. Conclusion

In this work, electrochemical nucleation, structural and magnetic behaviors of cobalt–copper electrodeposits obtained from a free-sulfate bath with boric acid was investigated. The effect of deposition potential on the properties of Co-Cu alloys thin films has been investigated by means of cyclic voltammetry, chronoamperometry, XRD and AGFM techniques. The experimental results show that the composition of Co-Cu electrodeposits varied with the deposition potential and the mechanism for formation of deposit is preceded growth by 3D crystallites. The deposits formed from all deposition potential a weak crystallization state and showed a mixture of Co fcc and hcp phases structure. AGFM measurements indicate that the films grown obtained at all applied potential have in-plane magnetic anisotropy and small coercivity.

References

[1] AE. Berkovitch, JR. Mitchell, MJ. Carey, AP. Young, FE.Spade, FT. Parker, A.Htten , G. Thonaas, Phys. Rev. Lett. 68 (1992) 3745.

[2] J. Xiao, J. Jiang and C. Chien, Phys. Rev. Lett. 68 (1992) 3749; Phys. Rev. B 46 (1992) 9266.

[3] Y. Chen, Y. Mei, R. Kaltofen, J. I. Mönch, J. Schumann, J. Freudenberger, H. J. Klauß, and O. G. Schmidt, Adv. Mater. 20, 3224 (2008).

[4]. J Q. Xiao, J S . Jiang , CL.Chien, ibid. 68 (1992) 3749.

[5] J . Yahalom, O. Zadok, J. Mater. Sci. 21 (1987) 499.

[6] H J. Blythe, VM. Fedosyuk, Phys. Stat. Sol. (a) 146 (1994) K13

[7] OF . Bakkaloglu, I H. Karahan, H. Efeoglu, M. Yildirim, U. Cevik , YK. Yogurtcu, J.Magn. Magn. Mater. 197 (1998) 53.

[8] H. Zaman, A. Yamada, H. Fukud ,Y. Ueda, J. Electrochem. Soc. 145 (1998) 565.

[9] P E. Brandley , D. Landlot, Electrochim. Acta 45 (1999) 1077.

[10] K. Miazaki, S . Kainuma, K. Hisatake, KT. Watanabe , N. Fukumuro, ibid. 44(1999) (21/22) 3713.

[11] SH. Ge, HH. Li, C. Li, L. Xi, W. Li, J. Chi, J. Phys.: Condens. Matter 12 (2000) 5905.

[12] GR. Pattanaik, SC. Kashyap, DK. Pandya, J. Magn. Magn. Mater. 219 (2000) 309.

[13] E. G'omez, A. Laberta, A. Llorente, E. Valléz, J. Electroanal. Chem. 517 (2001) 63.

[14] R. L´opez, J. Herreros, A. Gar'cia-arribasAR, JM. Barandiar'an, ML. Fdez-gubieda, J.Magn. Magn. Mater. 196 (1999) 53.

[15] JM. Doughton, J. Magn. Magn. Mater. 192(1999)334 __

[16] C P O. Treutler, Sens. Actuators, A, 9, 2 (200).

[17] GL. Zhou, MH. Yang,CP . Flynn, Phys. Rev. Lett. 77 (1996) 4580.

[18] PE. Brandly, D. Landlot, Electrochim. Acta 45 (1999) 1077.

[19] K. Miyazaki, S. Kainuma, K. Hisatake, T. Watanabe, N. Fukumuro, Electrochim Acta 44 (1999) 3713. [20] E. Gómez, A. Laberta, A. Llorente, E. Valléz, J. Electroanal. Chem. 517 (2001) 63.

[21] I. Bakonyi, ET. Kadar, J. Toth, LF. Kiss, L. Pogany, A. Cziraki, C. Ulhaq-Bouillet, V. Pierron-Bohnes, A. Dinia, B. Arnold, K. Wetzig. Europhysics. Letters 58 (2002) 408.

[22] I. Bakonyi, E. Toth-Kadar, A. Cziraki, J. Toth, LF. Kiss, C. Ulhaq-Bouillet, V. Pierron-Bohnes, A. Dinia, B. Arnold, K. Wetzig, P. Santiago, MJ. Yacaman. J. Electrochem. Soc. 149 (2002) 469.

[23] GR. Pattanaik, SC. Kashyap, DK. Pandya, J. Electrochem. Soc. 149 (2002) C363.

[24] JJ. Kelly, P. Kern, D. Landot, J. Electrochem. Soc. 147 (2002) 3725.

[25] R. López Antón, ML. Fdez-Gubieda, A. García-Arribas, J. Herreros, M. Insausti, Materials Science and Engineering A335 (2002) 94.

[26] T. Cohen-Hyams, WD. Kaplan, D.Aurbach, YS . Cohen, J. Yahalom, J. Electrochem. Soc. 150 (2003) C28.

[27] I. Bakonyi, J. Toth, LF. Kiss, E. Toth-Kadar, L. Peter, A. Dinia, J. Magn. Magn. Mater. 269 (2004) 156.

[28] M. R. Khelladi, L. Mentar, A. Azizi, M. Boubatra, A. Kahoul, Mater Chem Phys, 122 (2010) 449.

[29] M.R. Khelladi, L. Mentar, A. Azizi, A. Sahari, A. Kahoul, Mater Chem Phys 115 (2009) 385.

[30] Gu.M, Trans Inst Metal Finish 84 (2006) 4.

[31] S Fletcher,Electrochim Acta 28(1983) 917.

[32] E. Gomez, A. Labarta, A. Lorente, E. Valles, J. Electrochem. Soc. 151 (11) (2004) C731.

[33] G. Gunawardena, G. Hills, T. Montenegro,B. Scharifker, J. Electroanal. Chem. 138 (1982) 225.

[34] B. Scharifker, G. Hills, Electrochim. Acta 28 (1983) 879.

[35] A. Maeda, M. Kume, S. Oikawa, Y. Shimizu and M. Doi, J. Phys. (1993), p. 4641.

[36] TB, Massalski, Binary Alloy Phase Diagrams, ASM International, Materials Park, OH (1990).

[37] JW. Dini, Electrodeposition, p. 156; Noyes Publications, Park Ridge, NJ (1993).

[38] T. Cohen-Hyams, WD. Kaplan, J. Yahalom, Electrochem. Solid-State Lett., 5 (2002) C75.

[39] P. Nallet, E. Chassaing, MG. Walls, MJ. Hytch, J. Appl. Phys., 79 (1996) 6884.

[40] H. Safranek, "the Properties of Electrodeposited Metals and Alloys", New York (1991), p 63.

[41] L. Péter, A. Cziráki, L. Pogány, Z. Kupay,I. Bakonyi, M. Uhlemann,M. Herrich, B. Arnold, T. Bauer, K. Wetzig, J. Electrochem. Soc. 148 (2001) C168.

[42] BD. Cullity, Elements of X-ray Diffraction, vol. 91, 2nd Ed., Addison-Wesley, Reading, MA, 1978, 501.

Investigation of Impact Strength and Hardness of Aluminum based SiC Particle Reinforced Composites

P. Sundriyal[a] and V. K. Singh[b]

[a]M.Tech Scholar
[b]Associate Professor
Department of Mechanical Engineering
College of Technology, G. B. Pant University of Agri. & Tech., Pantnagar
Uttarakhand-263145, INDIA
Email: vks2319@yahoo.co.in, Phone: +919760825833

Abstract

Metal Matrix Composites have evoked a keen interest in recent times for potential applications in aerospace and automotive industries owing to their superior strength to weight ratio and high temperature resistance. Although several technical challenges exist with casting technology yet it can be used to overcome this problem. Achieving a uniform distribution of reinforcement within the matrix is one such challenge, which affects directly on the properties and quality of composite material. In the present study a modest attempt has been made to develop Aluminum based Silicon Carbide particulate. To achieve these objectives two step-mixing method of stir casting technique has been adopted and subsequent property analysis has been made. Aluminum 6063 series and Si-C (300 mesh) has been chosen as matrix and reinforcement material respectively. Experiments have been conducted by varying weight fraction of Si-C (7%, 14% and 21%), while keeping all other parameters constant. The results indicated that the 'developed method' is quite successful to obtain uniform dispersion of reinforcement in the matrix results obtained by microstructure test. An increasing trend of hardness and impact strength with increase in weight percentage of Si-C has been observed.

Keywords: SiC, Aluminium6063, Composites.

1. Introduction

Aluminum metal matrix composites (AMMCs) are superior to other metal matrix composites (MMCs) due to their low cost. There has been an increased interest in the use of composite materials in the recent past due to its unique physical and mechanical properties. AMMCs are increasingly used in aircraft, automotive components, structural and electronic applications and military industries [1-3].

Though MMCs possess superior properties they have not been widely applied due to their higher manufacturing cost and also due to poor machinability [4, 5]. The components made of these materials, can be produced by near-net shape manufacturing, they usually require subsequent machining to achieve the desired geometry, assembling tolerance and surface integrity [6, 7]. Main difficulties such as fabrication, machining and cost have to be overcome while applying composites in different applications [8, 9].

Aluminum 6063 series and Si-C has been chosen as matrix and reinforcement material respectively. Experiments have been conducted by varying weight fraction of SiC (7%, 14% & 21%), while keeping all other parameters constant. The aim involved in designing metal matrix composite materials is to combine the desirable attributes of metals and ceramics. The addition of high strength, high modulus refractory particle to a ductile metal matrix produces a material whose mechanical properties are intermediate between the matrix alloy and the ceramic reinforcement. Metals have a useful combination of properties such as high strength, ductility and high temperature resistance, but sometimes have low stiffness, whereas ceramics are stiff and strong, though brittle.

2. Material and method

In the present study sand casting process has been used for fabrication of metal matrix composite. Stir casting is opted for it. Sand is used as a refractory material in sand molding systems. Mollasses is used as binder that maintains the shape of the mould while pouring molten metal. Bentonite clay is used upto 4-10% of the sand mixture in Green sand systems, which is the most common sand casting system. Water, which makes up around 2-4% of the sand mixture, activates the binder. Carbonaceous material such as charcoal (2-10% of total volume) is also added to the mixture to provide a reducing environment. It helps in preventing the metal from oxidizing while pouring. The remaining 85-95% of the total mixture contains sand.

In the present study, coal fired furnace has been used. The crucible material was Graphite. Coal has been used as the fuel. A blower has been used for supplying the required quantity of air. Al 6063 is used as a matrix material and Si-C powder is used as filler material. We had made three composites of different compositions.

> 7% of Si-C in Al 6063 alloy
> 14% of Si-C in Al 6063 alloy
> 21% of Si-C in Al 6063 alloy

3. Result and discussion

Many In order to investigate change in properties of casted composites with the variation of Si-C we have performed the Microstructure test, Rockwell hardness test and Izod Impact test.

Microstructure

Microstructure is defined as the structure of a prepared surface or thin foil of material as revealed by a microscope above 25× magnification. The microstructure of a material (which can be broadly classified into metallic, polymeric, ceramic and composite) can strongly influence physical properties such as strength, toughness, ductility, hardness, corrosion resistance, high/low temperature behavior, wear resistance, and so on, which in turn govern the application of these materials in industrial practice. The microstructure of the composite has been observed with the help of Inverted Metallurgical Microscope: Figures 1, 2, 3, 4, 5 show the microstructures of the Al 6063, Si-C powder, Al 6063 with 7% SiC, 14% Si-C, 21%Si-C. Figure 1 & 2 shows the micro structure of pure Al 6063 and SiC and verified with the microstructure given in research work of Shorowordi K.M [10]. It has been observed that there are some changes in the microstructures. Figures 3, 4 and 5 depicts micrograph's of samples containing 7%, 14%, 21% SiC by weight respectively developed with the help of two-step mixing method of stir casting. It clearly shows the resulting homogeneous distribution of particles in the samples.

Figure 3 shows that clusters of Si-C particles in the primary α Al seemed to be finer. This can be explained by the fact that Si-C particles have a lower thermal conductivity and heat diffusivity than those of aluminum melt and therefore, Si-C particles were unable to cool down as they melt. As a result, the temperature of the particles was somewhat higher than liquid alloy. The hotter particles may heat up the liquid in their immediate surroundings, and thus delay solidification of the surrounding liquid alloy.
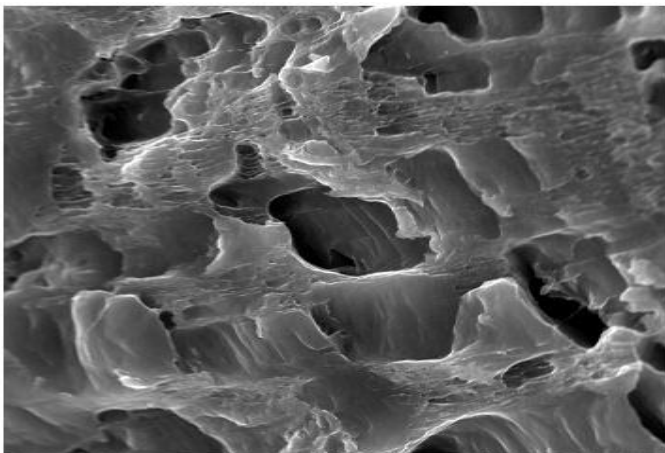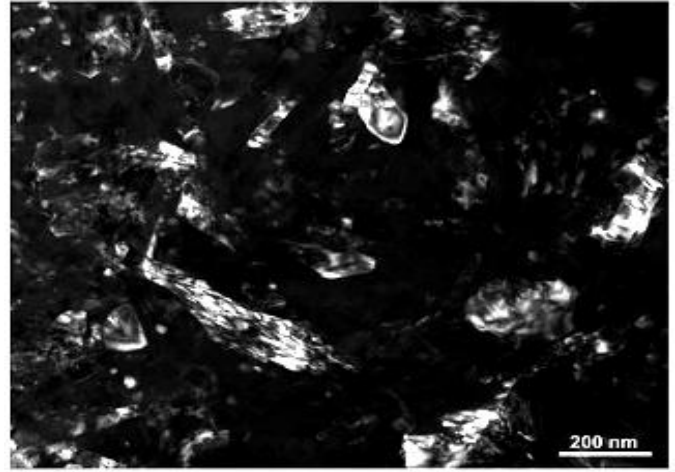

Figure 2: Si-C, (200+ magnification)

Figure 3: AL 6063 + 7% Si-C, (200+ magnification)

Figure 1: Al 6063 (200+ magnification)

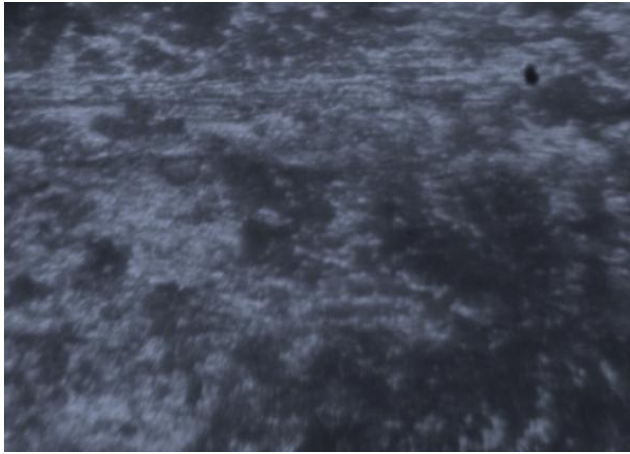Figure 4: Al 6063+ 14% Si-C, (200+ magnification)

Figure 5: AL 6063+21% Si-C, (200+ magnification)

Figure 4 & 5 show the extensive growth of the dendrites. During this growth, the freely suspended Si-C particles in the melt could either be entrapped by the dendrite front or pushed ahead by the front, depending on the velocity of the growing front and geometrical compatibility between the dendrite arm spacing and particle sizes. Pushing of particles by dendrite fronts could almost certainly occur if they were not entrapped. The existence of Si-C particles can result in instability in the growth front.

Hardness Test

As known, hardness implies a resistance to indentation, permanent or plastic deformation of material. In a composite material, filler weight fraction significantly affects the hardness value of the hybrid composite material. Hardness values measured on the Rockwell C-Scale showing the effect of weight percentage of Si-C on the hardness values of composite are presented in figure 6.

The Hardness of pure Al 6063 is 36 (HRC). Figure 6 shows that pure Al 6063 exhibits the lowest hardness amongst the entire composite studied. Addition of 7wt%, 14wt% and 21 wt% of Si-C particles increases 1.97, 2.06 and 2.17 times of hardness compared to pure Al 6063 respectively. It shows that hardness increases with increasing the Si-C particle.
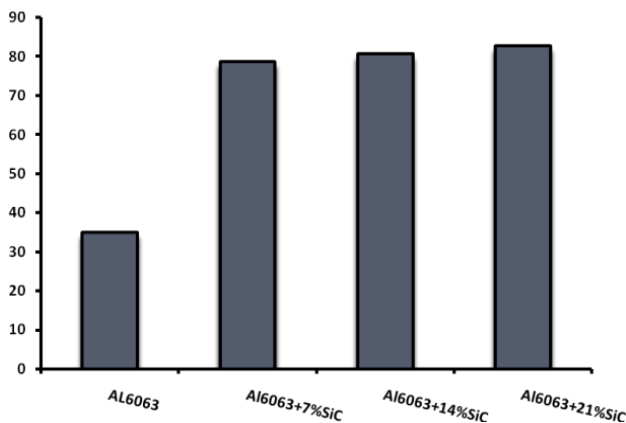

Figure 6: Variation of Hardness of composite Materials in HRC

Impact Test

For the impact testing, Izod test was performed on the notched specimens as recommended by ASTM standard for the rigid plastics. Specimen for this test had dimensions of 10x10x75mm3 as shown in figure 7. Three specimens of each type were tested in accordance with the same standard. The results obtained from the test are depicted in Figure 8.
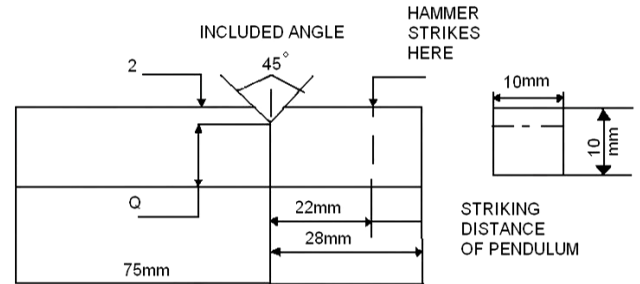

Figure 7: Specimens Geometry for Izod Test as per ASTM standard

The impact strength of pure Al 6063 is 16 Nm. Figure 8 shows that pure Al 6063 exhibits the lowest impact strength amongst the entire hybrid composite studied. Addition of 7wt%, 14wt% and 21 wt% of Si-C particles increases 31.25%, 43.75% and 75% of the impact strength as compared to pure Al 6063 respectively. It shows that impact strength increases with increasing the Si-C particle.
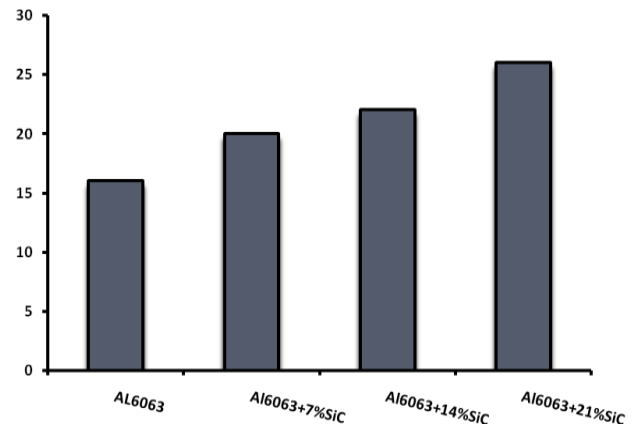
Figure 8: Variation of Impac tStrength of composite Materials in N-m

4. Conclusion

The results of experiment suggest that with increase in composition of Si-C, an increase in hardness and impact strength have been observed. With increase in composition of Si-C, the microstructures of the composites are more uniform. Homogenous dispersion of Si-C particles in the Al matrix shows an increasing trend in the samples prepared by stirring process.

Refrences

[1] K.M Shorowordi, T Laoui, A.S.M.A Haseeb, J.P Celis, L Froyen, Journal of Materials Processing Technology. (2003) 142: 738-743.

[2] O Quilgley, J Monaghan, P O'Reilly, Journal of Materials Processing Technology. (1994)43: 21-36.

[3] Sedat Ozden, Recep Ekici, Fehmi Nair, Composites: Part A. (2007) 38: 484-494.

[4] J.S Kwak, Y.S Kim. Journal of Materials Processing Technology. (2008) 20: 596-600.

[5] A Onat, H Akbulut, F Yilmaz, Journal of Alloys and Compounds. (2007)436: 375-382.

[6] M El-Gallab, M Sklad, Journal of Materials Processing Technology. (1998)83: 277 - 285.

[7] H Chandrasekaran, J.O Johansson, Annals of the CIRP. . (1997)46: 493-496.

[8] N.P Hung, F.Y.C Boey, K.A Khor., Y.S Phua, H.F Lee, Journal of Materials Processing Technology. (1996)56: 966-977.

[9] A Manna, B Bhattacharayya, Journal of Materials Processing and Technology. (2003)140: 711-716.

[10] K.M Shorowordi, T Laoui, A.S.M.A Haseeb, J.P Celis, L Froyen. Journal of Materials Processing Technology. (2003)142: 738-743

Characterization of the Fe$_{90-x}$Si$_{10}$Cr$_x$ (x=10, 15) nanostructured powders prepared by mechanical alloying

Z. Bensebaa[a], B. Bouzabata[b], A. Otmani[a], A. Djekoun[b] and J. M. Grenèche[c]

[a]Laboratoire de Recherche en Physico-chimie des Surfaces et Interfaces, Facultés des Sciences, Université de Skikda, B.P.26 Elhadack, Skikda.

[b] Laboratoire de Magnétisme et de Spectroscopie des Solides (LM2S), Département de Physique, Faculté des Sciences, Université de Annaba, B.P 12-23000 Annaba, Algérie

[c] Laboratoire de Physique de l'Etat Condensé, UMR CNRS 6087, Université du Maine, 72085 Le Mans, France.

Abstract

In this study, structural and magnetic properties of nanocrystalline Fe$_{80}$Si$_{10}$Cr$_{10}$ and Fe$_{75}$Si$_{10}$Cr$_{15}$ powders produced by mechanical alloying (MA) have been investigated and examined by X-ray diffraction and ^{57}Fe Mössbauer spectrometry. Mechanical alloying was carried out in a planetary high energy ball mill starting from pure elements of iron, silicon and chrome. After 15 h of milling, it is observed the formation of two bcc solid solutions α-Fe$_1$ (Si, Cr) and α-Fe$_2$ (Si, Cr) for the Fe$_{80}$Si$_{10}$Cr$_{10}$ alloy. Their grain sizes decrease with milling time and attains 23 nm and 11 nm respectively. For the Fe$_{75}$Si$_{10}$Cr$_{15}$ alloy the XRD shows the formation of the bcc and the cfc solid solution with a low concentration. The lattice parameter of the bcc solid solution increases with increasing time and chrome content. Mössbauer spectrum at room temperature of the Fe$_{80}$Si$_{10}$Cr$_{10}$ alloy resulted in the formation of two contributions, ferromagnetic and paramagnetic with a low concentration of 4 %. Addition of Cr as in the case Fe$_{75}$Si$_{10}$Cr$_{15}$ alloy increases the paramagnetic contribution with a relative concentration of 17.5 %.

Key-words: Nanocrystalline materials, Mechanical alloying, FeCrSi alloy, X-ray diffraction, ^{57}Fe Mössbauer spectrometry.
PACS:75. 50.Tt; 87. 20 Ev; 61. 10 Nz; 76.80+y.

1. Introduction

The nanostructured powders or particles with very fine crystalline grains can be synthesized by different techniques. In particular, the influence of nanometer grains on the structural and magnetic properties of these materials is intensively studied [1-3]. The mechanical alloying or high energy ball milling can be used conveniently to prepare nanostructured materials with often improved mechanical and magnetic properties [4]. The basic mechanism in milling elemental or prealloyed powders consists in a succession of fracture and welding that favors the formation of particles composed of nanometric grain size. The FeSiCr alloys have been subject of several studies related with their structural and magnetic properties [5, 6].

Addition of Si to Fe alloys enhances the electrical resistivity and therefore reduces the Eddy currents. And the addition of Cr in Fe-based alloys increases mechanical strength as well as oxidation and corrosion resistance at atmospheric and higher temperatures. Also, its magnetism under nanometer structure has been scarcely reported. It is interesting to examine the crystal structure and its corresponding magnetism as the mean grain size reduced down to a nanometer scale in the purpose of improving the magnetic properties of materials.

In this paper, the effect of milling time on the microstructure and magnetic properties were investigated for the nanocrystalline Fe$_{80}$Si$_{10}$Cr$_{10}$ and the Fe$_{75}$Si$_{10}$Cr$_{15}$ alloys prepared by mechanical alloying.

2. Experimental procedure

Mechanical alloying of the Fe$_{80}$Si$_{10}$Cr$_{10}$ and the Fe$_{75}$Si$_{10}$Cr$_{15}$ powders were carried out in a planetary high energy ball mill (Fritsch Pulverisette P7) starting from pure elements of iron, silicon and chromium, with different concentration. In all, mechanical milling was carried out at 400 rpm under argon atmosphere, using hardened steel balls and vials. The ball to powder weight ratio was 17:1. The milling times were: 5, 10 and 15 h. Structural changes were studied by X-ray diffraction (XRD) in a Philips diffractometer using CoKα$_1$ radiation (λ$_{Co}$ = 0.1788 nm). The structural and microstructural characteristics: lattice parameters, grain size and microstrains, were derived from the refinement of X-ray patterns using Maud program [7] based on the Rietveld method [8]. The ^{57}Fe Mössbauer spectra were performed at room temperature in a transmission geometry using a conventional constant acceleration spectrometer and fitted using the MOSFIT program [9]. All the isomer shifts were measured relative to a-iron at room temperature and a-iron was also used for calibration. The hyperfine parameters for these alloys were found by fitting the Mössbauer spectra.

3. Results and discussions

3.1 X-ray diffractions

Fig. 1. displays the XRD of the Fe$_{75}$Si$_{10}$Cr$_{15}$ powder as function of milling time. The best refinement of X-ray diffraction patterns of the powders is obtained with the isotropic model with full profiles of the diffraction peaks given by isotropic grain shape. The broadening of the diffraction peaks and the decrease in their heights with increasing milling time are due to the crystallite size refinement down to the nanometer scale and the increase of the internal strain. After 5 h of milling time, we

observed the formation of a disordered solid solution type bcc. At 10 h of milling, a disordered solid solution type cfc structure appears, this phase is clearly observed after 15 h of milling time a relative lower concentration of about to 12 %. Comparable results with the

presence of α-Fe (Si, Cr) and γ-Fe (Si, Cr) phases were also obtained in the ternary FeCrCo [10] and also in the binary FeCu [11].
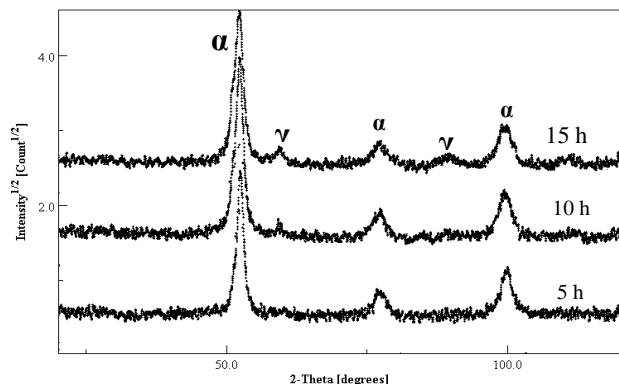

Fig. 1. XRD patterns of the $Fe_{75}Si_{10}Cr_{15}$ powders milled for various times.

Fig. 2. shown the variation of lattice parameter of phase α-Fe (Si, Cr) of the $Fe_{75}Si_{10}Cr_{15}$ powder during milling time. It is found that the lattice parameter varies little up to 5 h of milling. For milling times longer, there is an increase almost linearly with milling time. This increase may be related to the predominant distribution of chromium atoms (in higher concentration) in the solid solution α-Fe (Si, Cr) knowing that the atomic radius of chromium (R_{Si} = 0.185 nm) is higher than that of iron (R_{Fe} = 0.123 nm) [12].
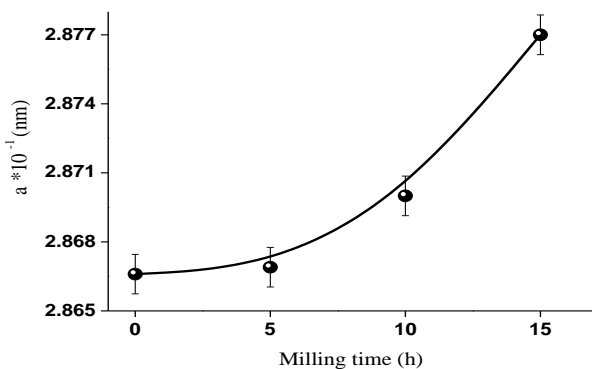

Fig. 2. Evolution of lattice parameters of the α-Fe (Si, Cr) solid solution of the $Fe_{75}Si_{10}Cr_{15}$ powder with milling time.

Fig. 3. show the Rietveld refinement of the XRD pattern of the ball-milled $Fe_{80}Si_{10}Cr_{10}$ powder mixture for 15 h. It is observed that the best fit of the diffractograms X Rietveld method is obtained using two disordered solid solutions: α1-Fe (Si, Cr) and α2-Fe (Si, Cr)-type bcc, with an average concentration on 90 % and 10 % respectively. The existence of the two bcc Fe structure can be assigned to the non-homogeneity in concentration of the milled $Fe_{80}Si_{10}Cr_{10}$ powder mixture leading the different diffusion process of Si and Cr

into the bcc Fe matrix induced by high energy ball milling. This effect does originate two types of atomic environments of Fe with different lattice parameters or/and grain size.
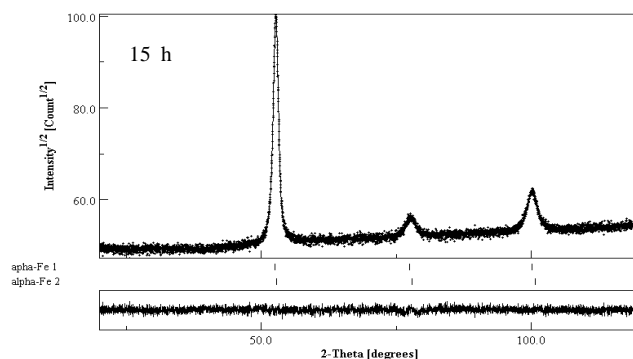

Fig. 3. Rietveld refinement of the XRD pattern of the ball-milled $Fe_{80}Si_{10}Cr_{10}$ powder mixture for 15 h.
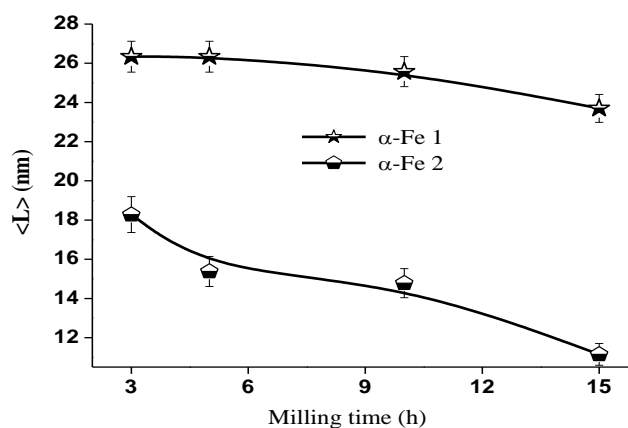

Fig. 4. Milling time dependence of the mean crystallite size for α-Fe 1 and α1-Fe 2 structures of the $Fe_{80}Si_{10}Cr_{10}$ powder.

Since the two bcc α-Fe structures have the different average crystallite <L>, Fig. 4. illustrated the variation of the crystallite size of the two solid solution with milling time. The crystallite size of both structures decrease to 23 and 11 nm respectively, after 15 h of milling. A similar result has been proposed in the nanostructured $Fe_{92}P_8$ alloy [13, 14] and in the FeCoAl alloy [15].

3.2 Mössbauer spectrometry analysis

The The Mössbauer spectra of $Fe_{80}Si_{10}Cr_{10}$ and $Fe_{75}Si_{10}Cr_{15}$ powders, taken at room temperature, for the 15 h of milling time and their hyperfine field distribution curves correspond are shown in Fig. 5. It is observed the spectrum of the $Fe_{80}Si_{10}Cr_{10}$ powder consists of sextet with broad lines characteristic of a disordered structure where iron atoms are largely replaced by atoms of silicon and/or chromium atoms and a singlet with a relative concentration of about 4 % correspond of paramagnetic phase. In the case of $Fe_{75}Si_{10}Cr_{15}$ powder, the Mössbauer spectrums have also composed of two contributions: one is ferromagnetic phase, consisting of sextet with broad lines due to the substitution of silicon and chromium, the second is a singlet paramagnetic phase with a relative concentration of 17.5%.

The hyperfine distributions $P(B_{hf})$ of the $Fe_{80}Si_{10}Cr_{10}$ can be unambiguously separate in tow regions: one with low fields and probabilities (< 20 T, H_2 (probable) = 17 T) and the other with high fields and probabilities (range 20-33 T, H_1 (probable) = 27 T), with a relative area ratio of 9 and 91%, respectively. This result is reported in detail in reference [16]. But the hyperfine field distribution curve $P(B_{hf})$ of the $Fe_{75}Si_{10}Cr_{15}$ powder milled for 15 h (Fig.5 .b) can be in fact, fitted with 4

Gaussians components, corresponding to 4 different domains, with values of magnetic fields. B_1 = 17 T can be a chromium-rich FeCr environment where iron atoms may have 5-7 chromium atoms on the two first coordination sphere, the value of B is comparable to that found in the ternary system FeCrCo and identical to that obtained in the binary FeCr [10]. B_2 = 22 T can be an environment (Fe, Si, Cr) rich in chromium and silicon.
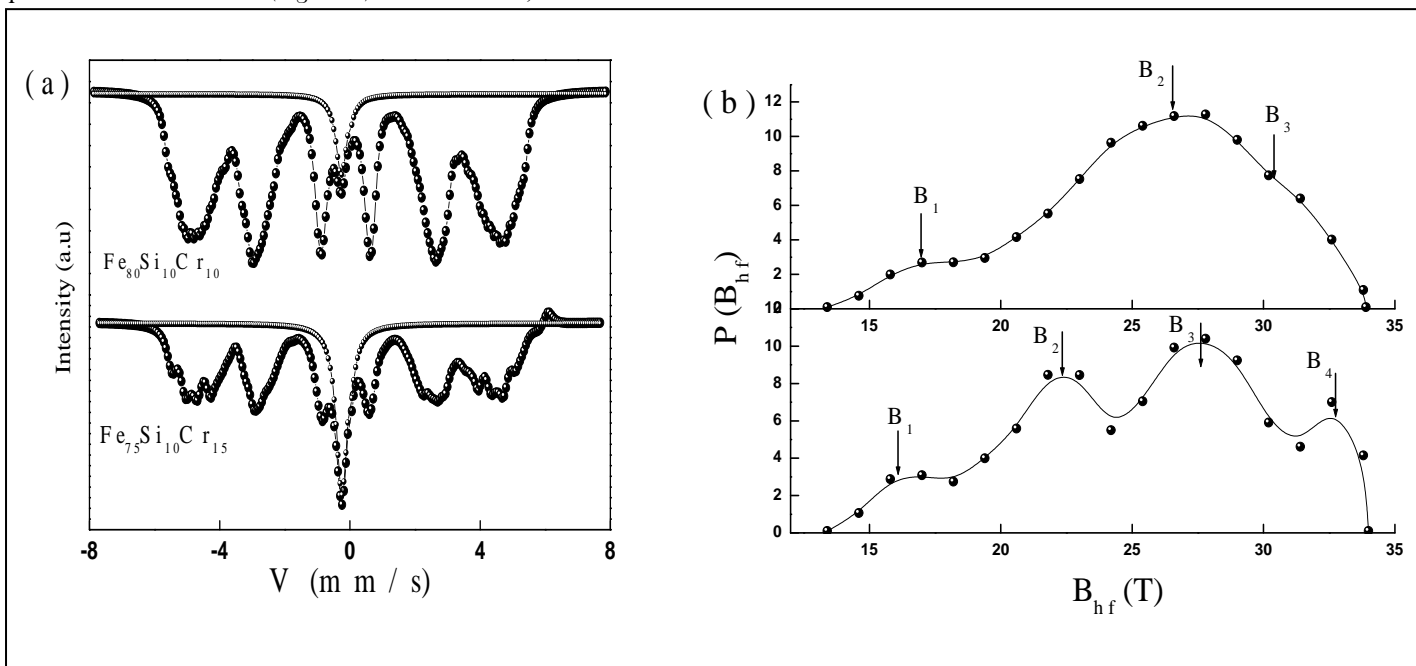

Fig. 5. Mössbauer spectra and the corresponding hyperfine field distribution $Fe_{80}Si_{10}Cr_{10}$ and the $Fe_{75}Si_{10}Cr_{15}$ powders milled 15 h.

B_3 = 28 T can be an environment (Fe, Si, Cr) rich in iron, where iron atoms are surrounded by two chromium atoms on the first two coordinations, or one atom of chromium and a silicon atom. B_4 = 32.7 T is probably an environment similar to that of pure iron which had is not alloyed with Si and Cr, with a relative fraction is 10 %.

Table 1.
Hyperfine parameters of the $Fe_{80}Si_{10}Cr_{10}$ and the $Fe_{75}Si_{10}Cr_{15}$ powders milled for 15 h.

Sample	Ferromagnetic phase		Paramagnetic phase	
	IS (mm/s)	<B> (T)	IS (mm/s)	%
$Fe_{80}Si_{10}Cr_{10}$	0,05	26,5	-0,09	4
$Fe_{75}Si_{10}Cr_{15}$	-0,02	22,5	-0,07	17,5

The hyperfine parameters deduced from the fitting of the Mössbauer spectra of the milled of the $Fe_{80}Si_{10}Cr_{10}$ and the $Fe_{75}Si_{10}Cr_{15}$ powders mixture for 15 h are summarized in Table1.

It can be inferred that the paramagnetic component appears in mixtures $Fe_{80}Si_{10}Cr_{10}$ and $Fe_{75}Si_{10}Cr_{15}$ powders increasing the chromium content. It is therefore possible that this phase is largely composed of Cr atoms substituted for iron.

4. Conclusion

The nanocrystalline alloys $Fe_{80}Si_{10}Cr_{10}$ and $Fe_{75}Si_{10}Cr_{15}$ were prepared by high energy nilling. The formation of these alloys has been followed by X-ray diffraction and Mössbauer spectroscopy.

In the case of the powder mixture of composition $Fe_{80}Si_{10}Cr_{10}$, the X-ray diffraction shows the formation of two solid solutions α1-Fe (Si, Cr) and α2-Fe (Si, Cr) after 15 h. Mössbauer spectra identify two magnetic components. The first is ferromagnetic and can be associated with the formation of two disordered solid solutions. As the second one, a paramagnetic type has a low relative concentration that increases with milling time (up to 4 % for 15 h).
In the case of the powder mixture $Fe_{75}Si_{10}Cr_{15}$, after 15 h of milling, there is the formation of a solid solution of bcc structure, with an average lattice parameter of about 0.287 nm and a cfc-type solid solution. The relative composition of this last paramagnetic phase is evaluated more precisely with Mössbauer spectra and is about 17. 5 %.

References

[1] H. Gleiter, Prog. Mater. Sci. 33(1989) 223.

[2] N.E. Fenineche, O. El Kedim, E. Gaffet, J. Meta, Nanocryst. Mater. (2000) 41.

[3] B. Zuo, T. Sritharan, Acta Mater. 53 (2005) 1233–1239.

[4] C. Suryanarayana, Progress Mater. Sci. 46 (2001) 1-184.

[5] Moon Suk Kim, Eui Hong Min, Jae Gui Koh, J.Magn. Magn. Mater. 321 (2009) 581-585.

[6] Reiko Sato Turtelli, Tibor Krenicky, Arbelio Penton-Madrigal, Roland Grossinger, Ivan Skorvanek, Herbert Sassik, Ernesto Estevez-Rams, Markus Schonhart, Carla da Fonseca Barbatti, J.Magn. Magn. Mater. 304 (2006) e687-e689.

[7] L. Lutterotti, MAUD CPD, Newsletter (IUCr) 24, 2000.

[8] H. M. Rietveld. J. Appl. Cryst. 2 (1969) 65.

[9] F. Varret, J. Teillet, Mosfit program, unpublished, 1976.

[10] F.Z. Bentayeb, S. Alleg, B. Bouzabata, J.M. Grenèche, J.Magn. Magn. Mater. 288 (2005) 282–296.

[11] O.Drbohlav and A.R.Yavari, Acta Metall.Mater. 43 (1995) 1799-1809.

[12] R. M. Tennent, Science Data Book, Olivier & Boyd, Hong Kong, (1971) 56-59.

[13] R. Bensalem, W. Tebib, S. Alleg, J.J. Sunˇol, L. Bessais, J.M. Grenèche, J. Alloys Compd. 471 (2008) 24–27.

[14] W. Tebib, S. Alleg, R. Bensalem, N. Bensebaa, F.Z. Bentayeb, J.J. Sunol, J.M. Grenèche, J. Nanosci. Nanotechnol. 8 (2008) 2029–2036.

[15] C. Djebbari, S. Alleg, J.M. Grenèche, Nuclear Instruments and Methods in Physics Research. B 268 (2010) 306-310.

[16] Z. Bensebaa, B. Bouzabata, A. Otmani, A. Djekoun, A. Kihal, J.M. Grenèche, J. Magn. Magn. Mater. 322 (2010) 2099–2103

Influence of Optical Kerr Nonlinearity on the Dynamic Behavior of Quantum Cascade Laser

A. Hamadou[a], Jean-Luc Thobel[b] and S. Lamari[c]

[a] Département ST, Institut des Sciences et de Technologies, Université El Bachir El Ibrahimi, Bordj Bou Arreridj, Algeria
[b] Institut d'Electronique, de Microélectronique et de Nanotechnologie (IEMN), UMR 8520, Université Lille 1, Avenue Poincaré, BP 60069, 59652 Villeneuve d'Ascq Cédex, France
[c] Département de Physique, Université Ferhat Abbas de Sétif, Algeria

Abstract

The effect of optical Kerr nonlinearity on the dynamic behaviors of quantum cascade laser operating in the mid-infrared is theoretically studied. Our model is based on three-level rate equations including the dependence of the loss on photon number in the cavity. The optical stability domain that allows for the determination of current injection is investigated. The equation that allow for the determination of the delay time is derived within the premises of our model in the most general case. Furthermore, nonlinear effects influence significantly the dynamics of photons in cavity and electrons in the upper laser level.

Key words quantum cascade laser; optical Kerr nonlinearity; dynamic behaviours; turn-on delay time; built-up time.

1. Introduction

Quantum cascade (QC) lasers [1] have gained more and more attention as unique coherent light sources in the mid-infrared. As opposed to conventional ones QC lasers present a fundamental advantage residing in their characteristic property consisting in the control of the wavelength of the emitted light via the layer thickness rather than the band gap. This allows for the emission wavelength of such a laser to be changed at will without resorting to a different semiconductor.

Optical Kerr nonlinearity effects have been studied and developed in intersubband transition in multi-quantum well structures by several authors [2-4]. The effects are due in mid-infrared to the large values of third order nonlinearities near a resonant intersubband transition [5-6]. The QC laser with saturable absorber mechanism due to Kerr effect has also been studied both theoretically and experimentally in recent years by using Maxwell-Bloch equations derived from semiclassical laser treatment when the laser operates in multimode regime [7-8].

In a QC laser the optical Kerr nonlinearity plays an essential role in the behaviour of optical media. A medium with optical Kerr nonlinearity can induce mode locking and thus lead to the generation of short lasers pulses [3]. On the other hand, the QC laser with optical Kerr nonlinearity leads to a photon number dependence of the losses and thus influences the static and dynamic behaviour regime [9]. Therefore, studies of QC laser with optical Kerr nonlinearity are important for potential applications in intersubband photonics field.

Our theoretical treatment laid below focuses only on the electrically injected three-level QC laser design proposed by H. Page [10] where lasing takes place through transitions from the upper state (level 3) to the lower state (level 2), and the latter being subsequently depopulated by longitudinal optical (LO) phonon emission into the ground state (level 1). Intersubband phonon scattering also occurs between levels 3 and 2, and 3 and 1, and is the main competing non-radiative process in mid-infrared QC lasers.

The aim of this work is to present numerically and analytically the effects of optical Kerr nonlinearity on the dynamic behaviours of QC laser operating in a single-mode.

2. Rate equation model

The QC laser rate equations with nonlinear Kerr effect for electron number N_3, N_2, and N_1 in levels 3, 2, and 1, and the photon number N_{ph} in the cavity can be written in the following form [9]:

$$\frac{dN_3}{dt} = WL\frac{J}{e} - \frac{N_3}{\tau_3} - \Gamma\frac{c'\sigma_{32}}{V}(N_3 - N_2)N_{ph}, \quad (1a)$$

$$\frac{dN_2}{dt} = \frac{N_3}{\tau_{32}} - \frac{N_2}{\tau_{21}} + \Gamma\frac{c'\sigma_{32}}{V}(N_3 - N_2)N_{ph}, \quad (1b)$$

$$\frac{dN_1}{dt} = \frac{N_3}{\tau_{31}} + \frac{N_2}{\tau_{21}} - \frac{N_1}{\tau_{out}}, \quad (1c)$$

$$\frac{dN_{ph}}{dt} = N\Gamma\frac{c'\sigma_{32}}{V}(N_3 - N_2)N_{ph} + N\beta\frac{N_3}{\tau_{sp}} - \frac{1}{\tau_p}\left(1 - \gamma_0 N_{ph}\right)N_{ph}. \quad (1d)$$

In the above system of equations, J denotes the electron current density that tunnels into the upper level and e is the electronic charge, while W and L are the lateral dimensions of the cavity, σ_{32} is the stimulated emission cross section between the upper and lower levels. Denoting by N and L_p the number of stages and length of each one of these, the whole volume V of the active area is then given by $NWLL_p$. In addition, in the above equations we introduced the mode confinement factor Γ and the average velocity of light in the system c' given by $c' = c / n_{eff}$ where n_{eff} and c are respectively the effective

refractive index of the cavity and the speed of light in vacuum whereas τ_p stands for photon lifetime and is determined by facet loss and waveguide loss of the cavity. The system dynamics is mainly determined by the three non-radiative scattering times denoted by τ_{32}, τ_{31}, and τ_{21} that are due to LO-phonon emission between the corresponding levels as well as by the radiative spontaneous relaxation time τ_{sp} between levels 3 and 2. Furthermore, between two adjacent stages we model the escape of electrons by a rate $1/\tau_{out}$ where τ_{out} stands for the electron escape time. To complete the picture, we take into consideration the proportion of spontaneous emission events that emit a photon into the cavity mode denoted by β [11]. For the sake of convenience, let us also introduce the lifetime τ_3 of the upper level which we write as $\tau_3 = \left(\tau_{32}^{-1} + \tau_{31}^{-1}\right)^{-1}$

The last term in Eq. (1d) models the nonlinear loss, per unit time, in the cavity due to the nonlinearity of the intersubband transition in quantum well. The nonlinear loss coefficient per unit time χ is obtained through the nonlinear refractive index n_2 [3], defined by $n = n_{eff} + n_2 I$ [3], where n is the refractive index, n_2 depends on the optical frequency detuning, and I is the light intensity in the cavity. I is related to the slowly varying envelope of the electric field E by $I = 2 n_{eff} \varepsilon_0 c E^2$, where ε_0 is the permittivity of vacuum.

Using the relation between the nonlinear loss coefficient per length and n, $\ell = n/(c\tau_p)$, one easily finds for $n_2 \langle 0$ the relation obtained in literature, $\ell = \ell_0 - \gamma E^2$ [7], where $\ell_0 = n_{eff}/(c\tau_p)$ is the linear loss coefficient per unit length and γ is called "self-amplitude modulation coefficient" [7] and related to the n_2 by $\gamma = 2 n_{eff} \varepsilon_0 n_2 / \tau_p$ [9].

Noting that $\chi_0 = c\ell_0/n_{eff}$ and $\chi = c\ell/n_{eff}$ and using the relation between the electric field and the number of photons $N_{ph} = 2\varepsilon_0 V E^2/(\hbar\omega)$, one easily finds the relation $\chi = \chi_0(1 - \gamma_0 N_{ph})$, where

$$\gamma_0 = \frac{c\tau_p \hbar\omega}{2 n_{eff} \varepsilon_0 V} \gamma , \qquad (2)$$

is the dimensionless coefficient which characterises the magnitude of nonlinear effects. In our simulations, we will consider γ_0 as the fundamental parameter.

In Eq. (2) $\hbar\omega$ is the photon energy, $\chi_0 = 1/\tau_p$ and the proportionality constant $c\tau_p \hbar\omega/(2 n_{eff} \varepsilon_0 V)$ is of the order of 5 V^2/m in the QC laser studied here.

In the following, we use in our calculation the parameters taken from Refs. [10-15]: τ_{21}=0.3ps, τ_{32}=2.1 ps, τ_3=1.4 ps, τ_p=3.36 ps, Γ=0.32, n_{eff}=3.27, N=48, W=34 µm, L=1 nm, L_p=45 nm, β=2×10^{-3}, σ_{32}=1.8×10^{-14} cm^2, and $N_{ph,sat}$=9.16×10^8.

In Ref. [9] we have found theoretically that the stable solution of photon number is given by

$$N_{ph,stat} = \frac{\left(-\gamma_0 N_{ph,sat} + 1\right)}{2\gamma_0} - \frac{\sqrt{\left(\gamma_0 N_{ph,sat} + 1\right)^2 - 4\gamma_0 N_{ph,sat} \dfrac{J}{J_{th}}}}{2\gamma_0} , \quad (3)$$

where $N_{ph,sat}$ is the photon saturation number given by [9,12]

$$N_{ph,sat} = \frac{1}{\tau_3(1 + \dfrac{\tau_{21}}{\tau_{31}})\Gamma \dfrac{c' \sigma_{32}}{V}} , \qquad (4)$$

and J_{th} denotes the threshold current density and given by[9]

$$J_{th} = \frac{e L_p}{\Gamma c' \sigma_{32} \tau_p \tau_3 (1 - \dfrac{\tau_{21}}{\tau_{32}})} . \qquad (5)$$

In Eq. (3), the normalized current injection verify the well-known optical stability domain (OSD) condition [9]

$$1 \langle \frac{J}{J_{th}} \langle \frac{1}{2} + \frac{\gamma_0 N_{ph,sat}}{4} + \frac{1}{4\gamma_0 N_{ph,sat}} = \left(\frac{J}{J_{th}}\right)_{max} , \quad (6)$$

where the quantity $(J/J_{th})_{max}$ is the endpoint of OSD. These results agree at least qualitatively with the recent experimental observations reported for 8 µm by Gordon *et al.* [7].

We show in Fig.1 the variation of the endpoint of OSD $(J/J_{th})_{max}$ as a function of the dimensionless parameter γ_0. It is worthwhile to stress the strong decrease of $(J/J_{th})_{max}$ as γ_0 increases from its minimal value 5×10^{-11} upward. The physical reason of this result is apparent: large detuning of the QC laser frequency away from resonance leads to high Kerr nonlinearity values, thereby suppressing the OSD to near zero.

In general, the lower the parameter γ_0, the more obvious threshold optical stability behaviour.

From these results it is easy to determine analytically the point where OSD will be lost by setting $(J/J_{th})_{max} = 1$ in Eq. (6). We have found that the system will lose OSD at $\gamma_0 = 1/N_{ph,sat}$. We can propose a possible experimental test of the effect by measuring the output power as a function of the current for different frequency detuning of the QC laser.
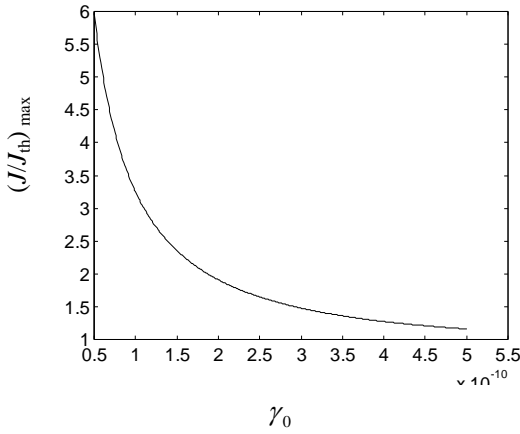
Fig.1. Endpoint of optical stability domain $(J/J_{th})_{max}$ as a function of the dimensionless coefficient γ_0

3. Dynamical behaviours

In the following we explore the temporal evolution of the population of levels N_1, N_2 and N_3, the population inversion ΔN, and the photon number N_{ph} under various values γ_0. We carry this out by solving the system of nonlinear differential equations given in Eqs.(1.a-d) using a 4th order Runge-Kutta method with an integration step $h_0 = 0.1$ ps and the following initial conditions $N_1(0) = N_2(0) = N_3(0) = N_{ph}(0) = 0$, the injection current J being finite and above threshold.

In Fig 2 we show the evolution of the electron number in the levels 3, 2, and 1 as a function of time for different values of γ_0, the results are all obtained for an injection current $J = 1.45 J_{th}$. We see that the electrons levels are quickly filled during the initial transient and then their population remains almost constant during a quite long period of time. After about 80 ps the number of electrons in the level 3 (level 2) decreases (increases) before reaching its stationary value depending on the value of γ_0: the higher the parameter γ_0 the lower (higher) the steady state value on level 3 (level 2). The steady state population in level 3 depends strongly on γ_0 as well as in level 2, while the steady state population in level 1 is independent of γ_0.
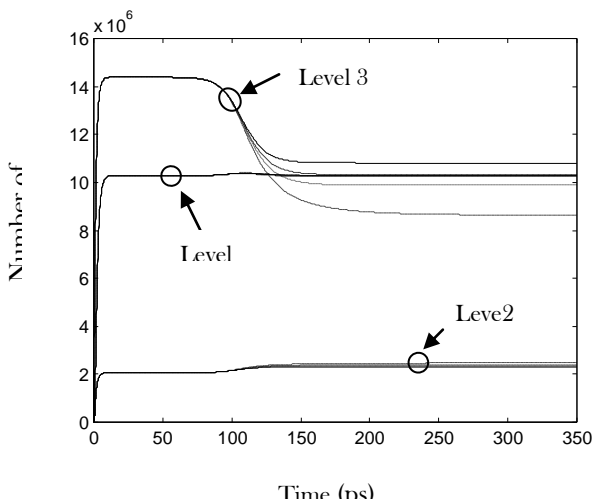

Fig.2. Time evolution of the number of electrons in the levels 3, 2 and, 1 of the QC laser for different values γ_0: Solid line ($\gamma_0 = 0$), dashed line ($\gamma_0 = 1.25 \times 10^{-10}$), dotted line ($\gamma_0 = 2 \times 10^{-10}$), and dash-dotted line ($\gamma_0 = 3 \times 10^{-10}$)

Fig.3. Time evolution of the photon number N_{ph} and population inversion ΔN for different values γ_0: Solid line ($\gamma_0 = 0$), dashed line ($\gamma_0 = 1.25 \times 10^{-10}$), dotted line ($\gamma_0 = 2 \times 10^{-10}$), and dash-dotted line ($\gamma_0 = 3 \times 10^{-10}$)
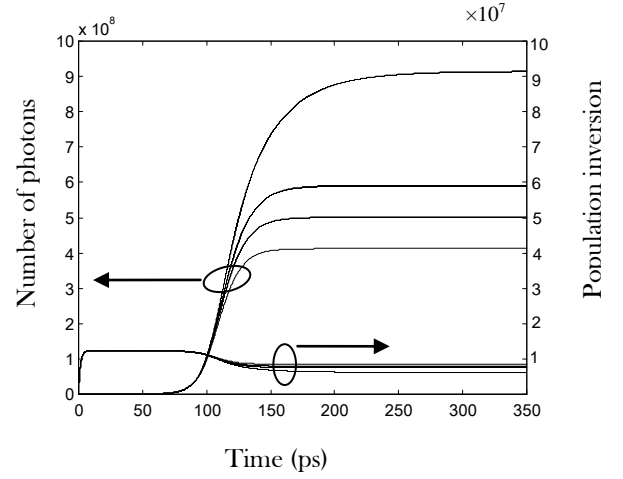
Figure 3 represents the time evolution of the photon number N_{ph} in the cavity. Also shown on the same figure is the population inversion ΔN between levels 3 and 2, the results are all obtained for an injection current $J = 1.45 J_{th}$. We can clearly see that the time needed to establish the stable stationary regime increases with increasing γ_0. As the results the delay time of QC laser increases with increasing of frequency detuning away from resonance.

Now, to compute the delay time t_d that elapses between the moment the bias is applied and the time the photon number reaches 10% of its stationary value we write $t_d \approx t_{th} + \Delta t_{10\%}$, where t_{th} is the turn-on delay time needed for the population inversion to reach its threshold value while $\Delta t_{10\%}$, the built-up time, is the interval of time where the number of photons is still very small. One proceeds in a manner strictly analogous to that of the Ref. [12], one gets

$$t_d \approx t_{th} + \frac{\tau_p}{\sqrt{\Delta}} \ln \frac{\dfrac{1}{10} N_{ph,stat} + \dfrac{\left(\dfrac{J}{J_{th}}-1\right)-\sqrt{\Delta}}{2\gamma_0}}{\dfrac{\left(\dfrac{J}{J_{th}}-1\right)-\sqrt{\Delta}}{2\gamma_0} + \dfrac{1}{10} N_{ph,stat} \dfrac{\left(\dfrac{J}{J_{th}}-1\right)-\sqrt{\Delta}}{\left(\dfrac{J}{J_{th}}-1\right)+\sqrt{\Delta}}}$$

$$(7)$$

where the time t_{th} is solution of the equation [12]

$$\frac{\xi_1 \exp(-\dfrac{t_{th}}{\tau_3}) - \xi_2 \exp(-\dfrac{t_{th}}{\tau_{21}})}{\xi_1 - \xi_2} = 1 - \frac{J_{th}}{J}, \qquad (8)$$

where the coefficients ξ_1 and ξ_2 are defined as [12]

$$\xi_1 = 1 + \frac{\tau_{21}}{\tau_{32}} \frac{1}{\dfrac{\tau_{21}}{\tau_3} - 1},$$

$$\xi_2 = \frac{\tau_{21}}{\tau_{32}} \frac{1}{1 - \dfrac{\tau_3}{\tau_{21}}}, \qquad (9)$$

and

$$\Delta = \left(\frac{J}{J_{th}} - 1 \right)^2 - 4\gamma_0 WL \frac{J}{e} \tau_3 \tau_p \frac{N\beta}{\tau_{sp}}. \qquad (10)$$

We show in Fig.4 the variation of the Built-up time as a function of the dimensionless coefficient γ_0 for normalized current density $J = 1.45 J_{th}$. It is found that Built-up time is an increasing function of γ_0.
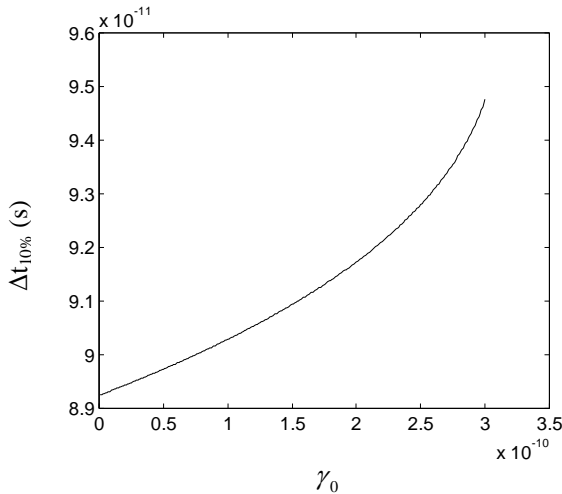

Fig.4. Built-up time variation versus coefficient γ_0

4. Conclusion

In summary, by using a simple rate equation model, we have investigated numerically and analytically the dynamic behaviours of a three-level mid-infrared QC laser in presence of optical Kerr nonlinearity. We have defined a dimensionless parameter γ_0, which characterises the magnitude of nonlinear effects. We have demonstrated that γ_0 can affect the optical stability domain dramatically. Numerical results show that the dynamic transient of electron in the upper laser level and photon in the cavity can be greatly modified by varying γ_0. We also developed an analytical scheme to derive the delay time as functions of γ_0, J and the different scattering times of the system.

References

[1] J. Faist, F. Capasso, D. L. Sivco, C. Sirtori, A. L. Hutchinson, A. Y. Cho, Science 264 (1994) 553-556.
[2] F. Capasso, C. Sirtori, A. Y. Cho, IEEE J. Quantum Electron 30 (1994) 1313-1326.
[3] R. Paiella, F. Capasso, C. Gmachl, D. L. Sivco, J. N. Baillargeon, A. L. Hutchinson, A. Y. Cho, H. C. Liu, Science 290 (2000) 1739-1742.
[4] J. Bai, D. S. Citrin, J. App. Phys 106 (2009) 031101-14.
[5] C. Sirtori, F. Capasso, D. L. Sivco, A. Y. Cho, Phys. Rev. Lett 68 (1992) 1010-1013.
[6] J. Bai, D. S. Citrin, IEEE J. Quantum Electron 43 (2007) 391-398.
[7] A. Gordon, C. Y. Wang, L. Diehl, F. X. Kärtner, A. Belyanin, D. Bour, S. Corzine, G. Höfler, H. C. Liu, H. Schneider, T. Maier, M. Troccoli, J. Faist, F. Capasso, Phys. Rev. A 77 (2008) 053804-18.
[8] A. Soibel, F. Capasso, C. Gmachl, M. L. Peabody, A. M. Sergent, R. Paiella, H. Y. Hwang, D. L. Sivco, A. Y. Cho, H. C. Liu, C. Jirauschek, F. X. Kärtner, IEEE J. Quantum Electron 40 (2004) 844-851.
[9] A. Hamadou, J.-L. Thobel, Opt. Commun 284 (2011) 2972-2979.
[10] H. Page, C. Becker, A. Robertson, G. Glastre, V. Ortiz, C. Sirtori, Appl. Phys. Lett 78 (2001) 3529-3531.
[11] M. Yamanishi, T. Edamura, K. Fujita, N. Akikusa, H. Kan, IEEE J. Quantum. Electron 44 (2008) 12-29.
[12] A. Hamadou, S. Lamari, J.-L. Thobel, J. App. Phys 105 (2009) 093116-6.
[13] A. Hamadou, J.-L. Thobel, S. Lamari, Opt. Commun 281 (2008) 5385-5388.
[14] S. Hofling, R. Kallweit, J. Seufert, J. Koeth, J.P. Reithmaier, A. Forchel, J. Cryst. Growth 278 (2005) 775-779.
[15] R. C. Iotti, F. Rossi, Rep. Prog. Phys 68 (2005) 2533-2571.

Structural and optical properties of CdSe doped KCl single crystal

L. Bouhdjer[a], S. Addala[a], A.b. Chala[b], O. Halimi[a], B. Boudine[a], M. Sebais[a] and S. Kara[a]

[a] Laboratory of Crystallography, Department of physics, Mentouri- University of Constantine, Constantine 25000, Algeria
[b] Laboratory Applied chemistry, Department of chemical, Mohamed Khaider- University of Biskra, Biskra 07000, Algeria

Abstract

Undoped and doped KCl single crystals by CdSe nanocrystals (NCs) have been grown by Czochralski (CZ) method with pulling rates in the 8-10 mm/h range. The crystals thus obtained were cleaved into samples of required size. The structural investigation of these samples has been deduced from Θ-2Θ(XRD) and Raman spectroscopy. The nano-size of CdSe aggregates in KCl host determined from XRD measurements by using the Sheerer formula. The Raman spectroscopy presented the LO mode vibration relative of (Cd-Se) chemical liaison. Moreover, the results of the optical absorption and photoluminescence spectra confirmed the nano-size of CdSe aggregates were observed band absorption located at 622,5nm relative of electronic transition 1se-1s3/2 of CdSe, with a blue shift from the bulk gap of $\Delta Eg=0,26eV$ (Eg (CdSe) bulk=1,73eV), while the photoluminescence showed a band situated at 643, 55 nm, with displacement Eg towards the short wavelength (blue shift), this bleu shift due to the nanometric size of CdSe aggregates.

Key words *nanocrystals, KCl single crystal, Cz method, XRD, Raman spectrometer, UV-Vis absorption, photoluminescence.*

1. Introduction

The II–VI semiconductors and in particular CdSe, with a suitable band gap of 1,74 eV, has attracted considerable attention due to the optical tenability over the entire visible range of the solar spectrum [1,2]. Hence there is a great technological interest in CdSe quantum dots for applications such as light emitting diodes [3], lasers [4], optoelectronic devices [5,6] and biological labels [7]. For their use, CdSe nanocrystals (NCs) can be dispersed into organic or inorganic matrix. The size, distribution and structural properties of nanocrystals strongly affect the performance and reliability of the constructed devices.

In the present paper, we report results of structural and optical study of KCl single crystals doped with CdSe nanocrystals (KCl:CdSe). Samples have been successfully grown using Czochralski method (Cz). The KCl host matrix has a wide band gap (Eg ≈ 6, 43 eV) which makes it transparent in the UV-Visible spectral range and allows to study the optical properties of CdSe nanocrystals in this range, it has been reported earlier for ZnO and CdS nanocrystals embedded respectively in single crystals of KBr and NaCl [8,9].

The charge carriers (excitons), in the semiconductor nanocrystals, are confined and the effect of confinement leads to fundamental changes in the electronic structure. When the particle size approaches the Bohr radius scale of exciton in bulk semiconductor, new optical properties appear [10]. These properties are highlighted in the present work.

2. Experimental details

KCl and KCl:CdSe single crystals were prepared using Cz method. Chemical reagents are KCl powder procured from "LABOSI/Chemicals products and reaction laboratory" with 99,9% purity, and CdSe nanopowder procured from "Aldrich chemicals" with 99,99% purity. The KCl:CdSe single crystals were prepared with starting materials 1 mol% of CdSe nanopowder (50nm) and 99 mol% of KCl. This mixture was heated to melting. The oven temperature has been controlled by the control system: Controller [REX-C100 SEPIES] and the platinum/platinum-Radium (10%) thermocouple. During the crystal growth, the pulling rates of 8 -10 mm/h and the rotation speed is about 1 round/mn are used along the operation.

The growth is carried out following the crystallographic axis [100]. The obtained crystals, with diameter of 2,5 cm and length of 7,5 to 10 cm, are cleaved parallel to the (100) plane in pellets with required size.

XRD data have been obtained using the Cu K_α radiation ($\lambda_{K\alpha}$ =1,5402 Å) and graphite filter of BRUKER-AXS D8 diffractometer. The structural composition of pellets was carried out by using a (Jobin-Yvon) µ-Raman spectrometer at room temperature (RT). Optical properties were analyzed using UV–Visible spectrophotometer (Shimadzu, UV-3101). Furthermore, the photoluminescence (PL) was measured at RT and the samples were excited by an argon laser (ionized light E_{exc}=514,5 nm) with an output power of 10 mW.

3. Results and discussion

XRD studies have been also performed on pure KCl single crystal in order to determine its structural state. Fig.1 shows the XRD diagram of a pure KCl single crystal. It exhibits three intense peaks at 2θ=28,48°; 2θ=58,78° and 2θ= 95° corresponding to plan (200) and its harmonics (400) and (600) respectively. This result shows that KCl crystal has cubic structure with the symmetry of Fm3m space group by referring to data of JCPDS 41-1476 file, discloses that the sample has single crystal character and confirms that the crystal was cleaved parallely to the (100) plan.
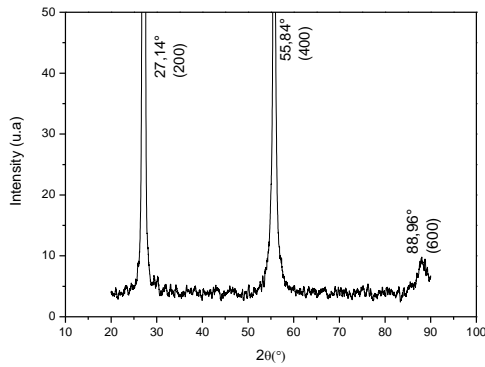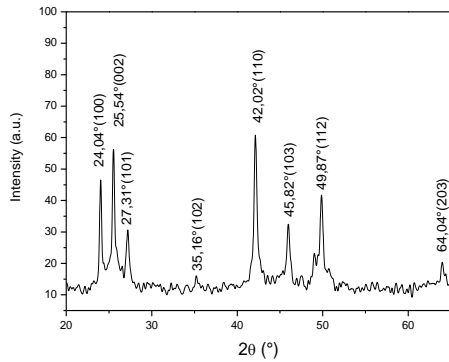
Fig. 1 XRD pattern of pure KCl single crystal

Fig. 2 XRD pattern of CdSe NCs.

The XRD spectrum of CdSe NCs, used for doping, is presented in figure 2. The good resolution and the high intensity of peaks indicate that CdSe NCs are of good crystalline quality. By comparing the positions of peaks with that of JCPDS 08-0459 file, we can deduce that CdSe NCs have hexagonal (wurtzite) structure with symmetry of space group P6₃mc.

Figure 3 displays the XRD spectrum of KCl:CdSe sample. It presents two peaks at $2\theta=28,7°$ and $2\theta=59°$ corresponding respectively to (200) and its harmonic (400) plans of KCl cubic structure. Moreover, it also reveals additional peaks with a weak intensity at $2\theta=23,35°$, $2\theta=25,52°$ and $2\theta=40,80°$. They are attributed respectively to the reflections (100), (002) and (110) of CdSe NCs. This result means the incorporation of CdSe NCs in the KCl single crystal.
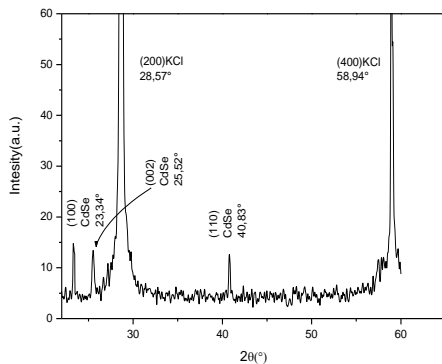

Fig.3 XRD pattern of KCl:CdSe single crystal.

For the size estimation of CdSe NCs, we have used the formula of Scherer (1) and the peaks have been fitted by Gaussian function.

$$D(nm) = \frac{0,9\,\lambda(nm)}{B(\theta)\cos(\theta)} \quad (1)$$

Where D is the crystallite diameter, λ the wavelength, θ the Bragg angle, $B(\theta)$ the full-width at half-maximum (FWHM) of the peak.

Table 1 presents the average sizes of CdSe crystallites embedded in KCl single crystal. The average radius found is about 45,34 nm.

(hkl)	(100)	(002)	(110)
2 θ (deg.)	23,35	25,52	40,80
FWHM (deg.)	00,17	00,23	00,16
D (nm)	47,66	35,41	52,96

Tabl.1: Average sizes of CdSe nanocrystals embedded in KCl single crystal

Fig.4 exposes Raman spectra of pure KCl and KCl:CdSe recorded at RT. They shows three peaks at 93,31 ; 141,12 and 183,87 cm^{-1} relative respectively to $T_{2g,2}$, $T_{2g,1}$ and A_{1g} Raman modes of KCl [11] these peaks are in the two spectra of KCl and KCl:CdSe. Furthermore there is an additional peak at 202,44 cm^{-1} in Raman spectrum of KCl:CdSe which is characteristic of phonon mode LO of CdSe [12-15]. It is known that the phonon mode LO of CdSe bulk crystal has a number wave of 213 cm^{-1}. But this peak shifts to the low energy side (up to 202,44 cm^{-1}) with decreasing CdSe NCs sizes due to phonon confinement and strain induced effects [16,17].
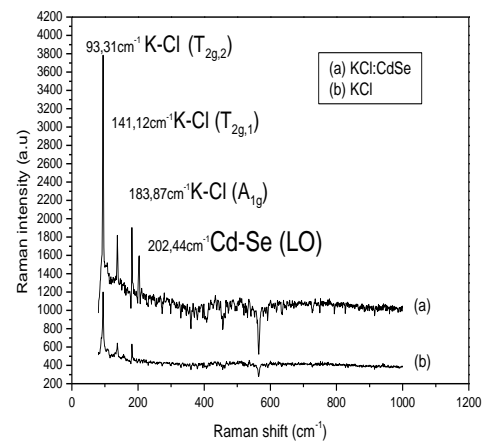

Fig 4: µ-Raman spectra: (a) pure KCl
(b) KCl:CdSe.

Optical absorption spectrum of pure KCl single crystal (Fig. 5(a)) shows that it is transparent in the visible region and has a strong absorption in the near ultraviolet. The absorption edge $E_g \approx 6,20$ eV is determined by the second derivative method [18] represented in Fig 5(b).
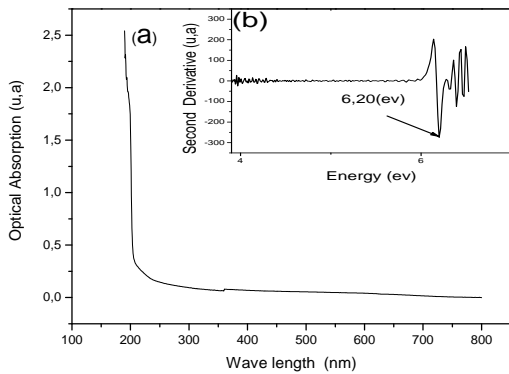
Fig. 5: Optical absorption spectra of KCl single crystal (a) and E_g of pure KCl (b).

Fig. 6(a) exhibits optical absorption spectrum of KCl:CdSe, which presents a band around 1,99eV (Fig. 6(b)) relative to the first absorption maximum ^1s_e-$^1s_{3/2}$ of CdSe according to work of S.V. Gaponenko [19]. It has been concluded from XRD patterns that the used CdSe powder has a wurtzite structure, whose bulk band gap energy is located at E_g = 1,73eV [20]. It appears a blue shift of band gap in value of $\Delta Eg=0,26eV$ for CdSe NCs in comparison to that of bulk CdSe in wurtzite structure. This shift of band gap energy was caused by the well known quantum confinement effect.
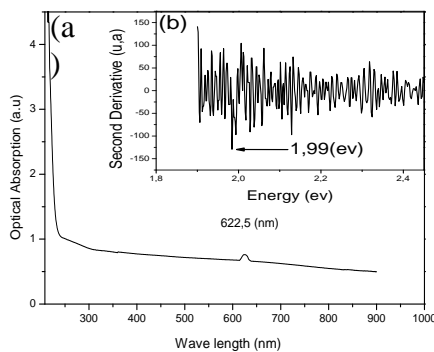

Fig. 6: Optical absorption spectra of KCl:CdSe single crystal (a) and the edge of CdSe NCs(b).

The photoluminescence (PL) spectrum of CdSe NCs embedded in KCl single crystal at RT is presented in Fig.7. It shows a broad emission band centered at 643, 55 nm which is consistent with optical absorption measurement. In comparison to the PL peak from wurtzite bulk CdSe, there is a blue shift ΔE_g= 0,19 eV due to quantum confinement effect. Moreover, the strong PL intensity from the KCl:CdSe can be attributed to the high crystalline quality of CdSe nanocrystals, which is in good agreement with the XRD patterns of CdSe powder discussed earlier. Therefore we can deduce that KCl single crystal is a suitable matrix to study the optical properties of CdSe NCs in UV-Visible range.
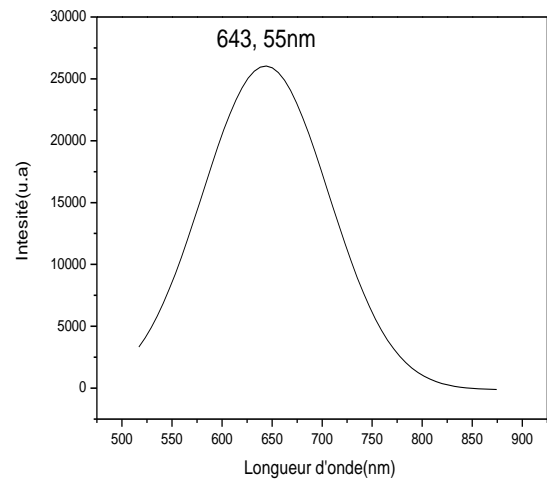

Fig. 7 Room temperature PL of KCl:CdSe single crystal.

4.   Conclusion

KCl single crystals, pure and doped with CdSe NCs, were prepared by Cz method. Structural characterization by XRD reveals the inclusion of CdSe NCs in KCl single crystal (host matrix) and shows that CdSe NCs have wurtzite structure. Furthermore KCl preserves its single crystal character. In addition, optical absorption spectra show a band located at 622,50 nm confirming CdSe NCs incorporation in KCl and demonstrates a blue shift of absorption edge ($\Delta Eg=0,26eV$) in comparison with CdSe bulk crystal. Photoluminescence of KCl:CdSe at RT shows a red luminescence band located at 643,55nm, with displacement to the short wavelengths (blue shift) which is due to the nanometric size of CdSe nanocrystals.

References

[1] D.J. Norris, A. Sacra, C.B. Murray, M.G. Bawendi, Phys. Rev. Lett. 72 (1994) 2612.

[2] M.G. Bawendi, A.R. Kortan, M.L. Steigerwald, L.E. Brus, J. Chem. Phys. 91 (1989) 7282.

[3] N. Matsumura, H. Endo, J. Saraie, Phys. Stat. Sol. B 229 (2002) 1039.

[4] M. Kazes, D.Y. Lewis, Y. Ebenstein, T. Mokari, U. Bannin, Adv. Mater. 14 (2002) 317.

[5] S. Coe, W.K. Woo, M.G. Bawendi, V. Bulovic, Nature (London) 420 (2002) 800.

[6] C.F. Hermandez, D.J. Suh, B. Kippelen, S.R.Marder, Appl. Phys. Lett. 85 (2004) 534.

[7] A. Urbieta, P. Fernandez, J. Piqueras, J. Appl. Phys. 96 (2004) 2210.

[8] O. Halimi, B. Boudine, M. Sebais, A. Challouche, R. Mouras, A. Boudrioua, J. Materials Science and Engineering C 23 (2003) 1111.

[9] B. Boudine, M. Sebais, O. Halimi, H. Alliouche, A. Boudrioua, R. Mouras, J. Catalysis Today 89 (2004) 293.

[10] O. Codo, A.G. Rolo, L.G. Vieira, M.J.M. Gomes, Ricolleau, D.J. Barber, J. Crystal. Growth 247 (2003) 371.

[11] A. de Andres and J.M. Calleja. J. Solid State Communications, Vo1.48,No.I1 (1983) 949-953.

[12] G. Jain-ping, L. Ya-dong, Y. Gou-qiang. Chinese Academy of Science, Beijing100101, China, 2002.

[13] S. Wageh, Physica E 39 (2007) 8–14.

[14] A.M. Alcalde, A.A. Ribeiro , N.O. Dantas , D.R. Mendes ,G.E. Marques, C. Trallero-giner : J. Non-Crystalline Solids 352 (2006) 3618–3623.

[15] Y. Badr, M.A. Mahmoud, Physica B 369 (2005) 278–286.

[16] R.W. Meulenberg, T. Jennings, G.F. Strouse, Phys. Rev. B 70 (2004) 235-311.

[17] P.A.M. Rodrigues, H. Cerdeira, F. Cerdeira, Int. J. Mod. Phys. B (1989) 1167.

[18] A. Othmani, J.C. Plenet, E. Berstein, C. Bovier, J. Dumas, P. Riblet, P. Gilliot, R. Levy, J.B. Grun, J. Crystal. Growth (1994) 144.

[19] S.V. Gaponenko, Optical Properties of Semiconductors, Cambridge University Press, Cambridge, 1998, p. 32.

[20] Y.-T. Nien et al. Materials Letters 62 (2008) 4522–4524.

Drimenin-rich essential oils from *Hertia cherifolia* growing in Algeria

A. Zellagui [a], N. Gherraf [a] and M. Lahouel [b]

[a] *Laboratory of Biomolecules and Plant Breeding, Life Science and Nature Department ,Faculty of Exact Science and Life Science and Nature , University of Larbi Ben Mhidi Oum El Bouaghi ,Algeria.*
[b] *Laboratory of Pharmacology and phytochemistry, Department of natural and life science, Faculty of Science, University Jijel, Algeria.*

Abstract

The hydrodistilled oil from crushed dry leaves of Hertia cherifolia which is endemic to Algeria and Tunisia collected from Ain Fekroun (Oum el Bouaghi, Algeria) were analyzed by gas chromatography-mass spectrometry to afford 36 components accounting for 99.3% of the total oil. the major components were found to be: Drimenin (67.5%), 1,2-Di(2-pyridinyl)-1,2-ethanediol (11.2 %), globulol(1.7 %), Cycloheptane, 4-methylene-1-methyl-2-(2-methyl-1-propen-1-yl)-1-vinyl- (1.5 %).
Key words *Hertia cherifolia, Essential oil, GC-MS, Drimenin*

1. Introduction

Essential oils have a complex composition, containing from a dozen to several hundred components. The great majority of components identified in essential oils includes terpenes (oxygenated or not), with monoterpenes and sesquiterpenes prevailing. Nevertheless, allyl- and propenylphenols (phenylpropanoids) are also important components of some essential oils [1], they can be synthesized by all plant organs (flowers, buds, seeds, leaves, twigs, bark, herbs, wood, fruits and root) and therefore extracted from these parts. The proportions of the components present in essential oils vary greatly. Major components can constitute up to 85% of the essential oils, while the remaining components can be present in only trace amounts [2]. Essential oils have many applications in folk medicine and for flavoring and preservation, as well as in the fragrance and pharmaceutical industries[2,3]. There has been a considerable interest in extracts and essential oils (EOs) from common culinary herbs, spices and aromatic plants, the Council of Europe describes "essential oil" as a product obtained from "vegetable raw material" [4]. Among many others, well-known families rich in essential oilsbearing species are asteraceae. Algeria is regarded as an important gene-centre for the family Asteraceae, it is an important sources of bioactive compounds and volatile oils, Genus *Hertia* comprises one species named *H.cherifolia* [5]. The aims of this study were to identify the chemical composition of essential oils isolated by hydro distillation the leaves of *H.cherifolia* grown in Algeria by gas chromatography/mass spectrometry (GC/MS) analysis.

2. Results and discussions

Table 1: Chemical composition of *H.cherifolia* essential oil

Constituents	Rt	%
6- α -Elemene	11.26	0.6
β -Caryophyllene	12.06	0.9
Humulene	12.97	0.4
Nopol	13.40	0.2
Eremophilene	13.58	0.7
α -Eudesmene	13.73	1.0
Valencene	13.80	0.7
α-Selinene	13.96	0.5
α-Murolene	14.11	0.1
Butylated Hydroxytoluene	14.21	1.0
α-Cubebene	14.34	0.3
Cadinene	14.57	0.8
Spathulenol	15.35	1.1
Cycloheptane, 4-methylene-1-methyl-2-(2-methyl-1-propen-1-yl)-1-vinyl-	15.43	1.5
Davanone	15.72	0.9
5-Pentadecen-7-yne, (Z)-	15.85	0.3
Propane, 1-chloro-3-diethylboryloxy-2,2-dimethyl	15.97	0.4

(Z,E)-α-Farnesene	16.43	0.5
Aromadendrene, dehydro-	16.84	0.2
1,10-Dimethyl-2-methylene-trans-decalin	16.97	0.7
Cycloisolongifolene	17.11	0.1
Benzene 1,1-diethylpropyl	17.34	3.4
(2S,4R)-p-Mentha-[1(7),8]-diene 2-hydroperoxide	17.40	0.1
2,2,4-Trimethylchromene-3	17.57	0.1
Bicyclo2.2.2.octane1,2,3,6-tetramethyl	17.70	0.3
Cyclopentanecarboxaldehyde, 2-methyl-3-methylene-	17.79	0.2
Tricyclo[4.4.0.0(2,7)]dec-3-ene-3-methanol, 1-methyl-8-(1-methylethyl)-	17. 95	0.1
1-(1-Ethyl-2,3-dimethyl-cyclopent-2-enyl)-ethanone	18.02	0.1
1,2-Ethanediol, 1,2-di-2-pyridinyl-	18.46	**11.2**
Drimenin	18.51	**67.5**
1-(6-Methyl-2-pyrazinyl)-3-methyl-1-butanol	18.65	0.3
Ethyl phthalyl ethyl glycolate	19.08	0.1
Decane-1-sulfonic acid (4-methoxy-phenyl)-amide	19.75	0.1
Cycloisolongifolene, 8,9-dehydro-9-formyl	21.06	1.1
Benzo[g]pteridine, 2,4-diamino-6,7,8,9-tetrahydro-7-methyl-	21.45	0.1
globulol	23.57	**1.7**
Total identified		99. 3%

Sesquiterpene hydrocarbons	8.3
Oxygenated monoterpenes	0.3
Oxygenated sesquiterpenes	72.3
others	18.4

The essential oils components identified are listed in Table 1, together with their relative percentages, in order of their retention times. The qualitative composition of the leaves yields thirty six components representing 99.3%. This report is the first study of the composition of the essential oils obtained from the leaves in vegetative stage of *H.cherifolia* growing in Algeria.

The essential oils(yield 0.02%, w/w) was mainly composed of with Drimenin (**67.5** %) as the major constituent, this is specific only in this species.

The main constituent of the essential oilsfrom the leaves was Drimenin (67.5%), 1,2-Di(2-pyridinyl)-1,2-ethanediol (11.2 %), globulol(1.7 %), Cycloheptane, 4-methylene-1-methyl-2-(2-methyl-1-propen-1-yl)-1-vinyl- (1.5 %).

Concerning the chemical composition of the essential oilsof other *Hertia* species, Afsharypuor *et al.* [6] showed that the oil of the aerial parts of Hertia angustifolia composed of the b-pinene (51.5%), b-phellandrene (16.5%), a-pinene (13.9%) and a-thujene (2.7%), as the main constituents. Also reported that the of the aerial parts of Hertia cheirifolia collected in aures – Algeria was characterized by contents Eremophilenolide-Type Sesquiterpenes isolated from chloroform and methanolic extract [7,8,9,10].

Hence, the composition of the essential oilsof the leaves of *H.cheirifolia* was very different from that of all the *Hertia* species studied so far. The compound that mostly characterized this species was (-)-Drimenin.

3. Experimental

3.1. Plant material and isolation

The leaves of *H.cherifolia* were collected during February 2010 (vegetative stage) in Oum el bouaghi, Algeria. The plants were identified by Dr Zellagui Amar and a voucher specimen was deposited in the Laboratory of Biomolecules and Plant Breeding, University of Larbi Ben Mhidi Oum under number ZA 122.

Fresh leaves (100g) were hydrodistilled in a Clevenger-type apparatus for 3 h.

3.2. Gas chromatography- mass spectrometry

Analyses were performed with a Varian CP-3800 gas chromatograph equipped with a DB-5 capillary column (30m × 0.25 mm; coating thickness 0.25 µm) and a Varian Saturn 2000 ion trap mass detector. Analytical conditions: injector and transfer line temperatures 220 and 240°C, respectively; oven temperature programmed from 60°C to 240°C at 3°C/min; carrier gas helium at 1 mL/min; injection 0.2 µL (10% *n*-hexane solution); split ratio 1:30. Identification of the constituents was based on comparison of the retention times with those of authentic samples, comparing their linear retention indices relative to the series of *n*-hydrocarbons, and by computer matching against commercial (NIST 98 and ADAMS) and homemade library mass spectra built up from

pure substances and components of known oils and MS literature data [11].

4. Conclusion

H.cheirifolia investigated for the first time in Algeria for essential oil. The analysis of the essential oils revealed that this essential oilsis rich in Drimenin because of the high content, this essential oilsmay become a source of this substance.

References

[1] C.M.F. Cavaleiro, Óleos essenciais de Juniperus de Portugal. PhD Thesis, Universidade de Coimbra, Faculdade de Farmácia, Coimbra, Portugal, 2001.

[2] M.G. Miguel, Antioxidant activity of medicinal and aromatic plants. Flavour Fragr. J. 25 (2010) 291-312.

[3] N.S. Sangwan, A.H.A. Farooqui, F. Shabih, R.S. Sangwan, Regulation of essential oilsproduction in plants. Plant Growth Regul. 34 (2001) 3-21.

[4] Anonymous Natural Sources of Flavourings. Report no 1. Council of Europe Publishing, Strasbourg 2000.

[5] S.B. Afsharypuor, M.J. Maryam; M.R. Rahiminezhads, F. Daru, Investigation of the volatile oil of Hertia angustifolia (DC.) O. Kuntze), , Journal of Faculty of Pharmacy, Tehran University of Medical Science 8(1 & 2) (2000) 7-8.

[6] P. Quezel, S. Santa. Nouvelle Flore de L'Algérie et des Régions Désertiques Méridionales. Tome II. Editions du Centre National de la Recherche Scientifique (C.N.R.S), 15 Quai Anatole France, Paris 1963.

[7] S. Ammar; H. Edziri,; M. A. Mahjoub, R. Chatter, A. Bouraoui, Z. Mighri, Spasmolytic and anti-inflammatory effects of constituents from Hertia cheirifolia, Phytomedicine 16(12) (2009) 1156-1161

[8] P. Aclinou, G. Massiot. Absolute configuration of eremophilenolides from Hertia cheirifolia Phytochemistry, 4(3) (1993) 859-60.

[9] P. Aclinqu,; A. Benkoudier, G. Massiot, L. L. Men-Olivier, Plants from Aures. Part 5. Eremophilenolides from Hertia cheirifolia Phytochemistry 30(6) (1991) 2083-4.

[10] G. Massiot, J. M. Nuzillard, L. L. Men-Olivier, P. Aclinqu, A. Benkoudier, Plants from Aures. Part 4. Eremophilenolides from Hertia cheirifolia.Phytochemistry, 29(7) (1990) 2207-10

[11] P. Adams. Identification of Essential oilsComponents by Gas Chromatography/Mass Spectrometry, 4th Ed. Allured Publishing Corporation. Carol Stream, Illinois, 2007.